Journal of Computational Physics 228 (2009) 3048–3071

Contents lists available at ScienceDirect

Journal of Computational Physics

journal homepage: www.elsevier.com/locate/jcp

A new combined stable and dispersion relation preserving compact scheme for non-periodic problems

T.K. Sengupta *, V. Lakshmanan, V.V.S.N. Vijay

Department of Aerospace Engineering, Indian Institute of Technology Kanpur, I.I.T. Kanpur, U.P. 208016, India

ARTICLE INFO

Article history:
Received 25 April 2008
Received in revised form 19 December 2008
Accepted 8 January 2009
Available online 16 January 2009

Keywords:
Combined compact difference scheme
DRP property
Uni-and bi-directional wave propagation
Stommel Ocean model
Navier–Stokes solution
Lid-driven cavity problem
Boundary layer

ABSTRACT

A new compact scheme is presented for computing wave propagation problems and Navier–Stokes equation. A combined compact difference scheme is developed for non-periodic problems (called NCCD henceforth) that simultaneously evaluates first and second derivatives, improving an existing combined compact difference (CCD) scheme. Following the methodologies in Sengupta et al. [T.K. Sengupta, S.K. Sircar, A. Dipankar, High accuracy schemes for DNS and acoustics, J. Sci. Comput. 26 (2) (2006) 151–193], stability and dispersion relation preservation (DRP) property analysis is performed here for general CCD schemes for the first time, emphasizing their utility in uni- and bi-directional wave propagation problems – that is relevant to acoustic wave propagation problems. We highlight: (a) specific points in parameter space those give rise to least phase and dispersion errors for non-periodic wave problems; (b) the solution error of CCD/NCCD schemes in solving Stommel Ocean model (an elliptic p.d.e.) and (c) the effectiveness of the NCCD scheme in solving Navier–Stokes equation for the benchmark lid-driven cavity problem at high Reynolds numbers, showing that the present method is capable of providing very accurate solution using far fewer points as compared to existing solutions in the literature.

1. Introduction

Compact difference schemes have been proposed for applications requiring high accuracy computing [1–6]. These schemes approximate operators using implicit stencils with relatively large grid spacing, due to their spectral-like resolution [1]. Compact schemes require fewer grid points, due to favorable properties of numerical stability and dispersion relation preservation (DRP) [3,5,14]. In these references, various schemes have been analyzed for DRP property in terms of numerical group velocity for wave propagation problems [7–9].

Compact representation can be obtained separately for first and second derivatives (as in [1]), or the derivatives can be obtained simultaneously using Hermitian polynomials [2,10–12]. These schemes are referred to as the CCD schemes [2,6,11]. The second derivative can also be computed by applying twice the compact schemes for evaluating first derivative. This however, leads to poorer scale resolution at high wave numbers and therefore is not recommended. In many of the cited references, a rudimentary analysis depicting scale resolution of the schemes based on Fourier series representation is provided [1,11]. The analysis in [3–5,14] is an exception, where additional properties fixing phase and dispersion errors are obtained with the help of numerical group velocity and phase speed. The same analysis is performed here for the CCD schemes for the first time.

* Corresponding author. Tel.: +91 512 2597945; fax: +91 512 2597561.
E-mail address: tksen@iitk.ac.in (T.K. Sengupta).

0021-9991/$ - see front matter © 2009 Elsevier Inc. All rights reserved.
doi:10.1016/j.jcp.2009.01.003

Computations for simulating complex physics problem do not always fully explain the causality. Whether such failures are due to the complexity arising out of space–time dependent nonlinear dynamics and/or inadequacy of the computing method is not fully understood yet. A recent study [14] identified mechanisms for solution breakdown of linear equation to be related to numerical properties – those have been attributed earlier to nonlinearities. CCD schemes for non-periodic problems also require a thorough analysis for wave propagation problems. For this purpose, we look at the one-dimensional linear convective equation,

$$\frac{\partial u}{\partial t}+c\frac{\partial u}{\partial x}=0,\quad c>0. \tag{1}$$

This is an example of signal propagation, where the solution convects downstream without dispersion. The inaccuracy of the computed solution for this problem is not due to nonlinearity – although not all the aspects of the solution are revealed – as noted in [9]. Recently it is reported in [14] that the loss of accuracy is due to common properties shared by all discrete computational methods. The method for analyzing discrete methods with Fourier–Laplace transforms [5,14] is invoked in this paper. This provides a yardstick to compare disparate methods. The unknown is expressed in the wave number (k) plane by, $u(x,t)=\int U(k,t)e^{ikx}dk$, such that an amplification factor can be introduced as $G(k)=U(k,t+dt)/U(k,t)$. For direct numerical simulations one must have a neutrally stable method. For Eq. (1) the group velocity (V_g) is equal to the phase speed c and this physical principle must be obeyed by any numerical method. The analysis for any discrete computation shows that the numerical solution u_N satisfies a different equation. More specifically, the constant c, becomes wave number dependent. It is important to correctly define the numerical error as $e=u-u_N$, as is shown in [14]. In most of the text books and monographs (as in [13,16]), the error is defined as the difference between a fictitious exact solution of the discrete equation and the numerical solution. In the process, it is wrongly concluded that the same discrete equation is followed by the solution and the error. The correct error propagation equation is given by [14],

$$\frac{\partial e}{\partial t}+c\frac{\partial e}{\partial x}=-c\left[1-\frac{c_N}{c}\right]\frac{\partial \bar{u}_N}{\partial x}-\int\frac{V_{gN}-c_N}{k}\left[\int ik'A_0[|G|]^{t/\Delta t}e^{ik'(x-c_Nt)}dk'\right]dk-\int\frac{Ln|G|}{\Delta t}A_0[|G|]^{t/\Delta t}e^{ik(x-c_Nt)}dk. \tag{2}$$

In the above, $A_0(k)$ denotes the Fourier amplitude of the initial condition and c_N is the numerical phase speed. One notes that Eq. (2) is very generic and exact – unlike the one obtained using modified equation approach [15–20]. In modified equation approach, one accounts for truncation error by collating and representing the discretized terms in the difference equation by their equivalent differential forms. The resultant modified equation depends upon the method of discretization. In contrast, Eq. (2) clubs error based on generic stability and DRP properties.

If a numerical scheme is neutrally stable, then the last term on the right-hand side of (2) would not be present. The first term on the right-hand side of (2) is due to phase error, with respect to the mismatch between numerical and actual phase speed. The second term on the right-hand side quantifies the spurious dispersion effect created by numerical methods. Eq. (2) replaces the widely used von Neumann stability analysis given in [21,22] as the correct error propagation equation. This feature of scientific computing is unique and not shared by any analytical methods of mathematical physics and is brought out the first in [14].

In view of the above, one would estimate the properties of CCD in solving both the uni-directional and bi-directional wave problems. In the former, one requires very accurate first derivatives, while in the latter the second derivatives have to be correct. The paper is formatted in the following manner. In the next section, analysis of CCD schemes is presented for non-periodic problems and some stability problems of CCD schemes are identified which are related to boundary closures. In Section 3, NCCD scheme is developed and used in solving uni- and bi-directional wave propagation problems with non-periodic boundary conditions. In Section 4, the results for the Stommel Ocean model using the present NCCD scheme are reported. The development of a boundary layer over a flat plate and the flow inside a lid-driven cavity are investigated in Section 5 by solving Navier–Stokes equation, as an illustration of NCCD scheme's utility in solving initial-boundary value problems.

2. Combined compact difference (CCD) scheme for non-periodic problem

The CCD schemes described in [2,11] obtain simultaneously the first and second derivatives (f'_j, f''_j), in terms of the function (f_j) defined in a uniform grid of spacing h, from the following discrete equations for $j=2$ to N:

$$\frac{7}{16}(f'_{j+1}+f'_{j-1})+f'_j-\frac{h}{16}(f''_{j+1}-f''_{j-1})=\frac{15}{16h}(f_{j+1}-f_{j-1}), \tag{3}$$

$$\frac{9}{8h}(f'_{j+1}-f'_{j-1})-\frac{1}{8}(f''_{j+1}+f''_{j-1})+f''_j=\frac{3}{h^2}(f_{j+1}-2f_j+f_{j-1}). \tag{4}$$

If we consider Dirichlet boundary conditions at $j=1$ and $N+1$ then there are $2N+2$ unknown derivatives, with four unknowns contributed from the nodes at $j=1$ and $N+1$ for the derivatives. Thus, one would require four additional equations and in [2] they were given by,

$$f'_1 + 2f'_2 - hf''_2 = \frac{1}{h}(-3.5f_1 + 4f_2 - 0.5f_3), \tag{5}$$

$$hf''_1 + 5hf''_2 - 6f'_2 = \frac{1}{h}(9f_1 - 12f_2 + 3f_3), \tag{6}$$

$$f'_{N+1} + 2f'_N + hf''_N = \frac{1}{h}(3.5f_{N+1} - 4f_N + 0.5f_{N-1}), \tag{7}$$

$$hf''_{N+1} + 5hf''_N + 6f'_N = \frac{1}{h}(9f_{N+1} - 12f_N + 3f_{N-1}). \tag{8}$$

The multiplicative constants in the above equations are fixed by matching Taylor series expansion coefficients up to the sixth order. Thus, we have a complete linear algebraic system for the evaluation of first and second derivatives. We express the function in spectral plane to compare scale resolution ability of different methods.

The exact first spatial derivative of u is given by, $[\frac{\partial u}{\partial x}]_{exact} = \int ikUe^{ikx_j}\,dk$. Discrete computing methods obtain the same spatial derivative u' by,

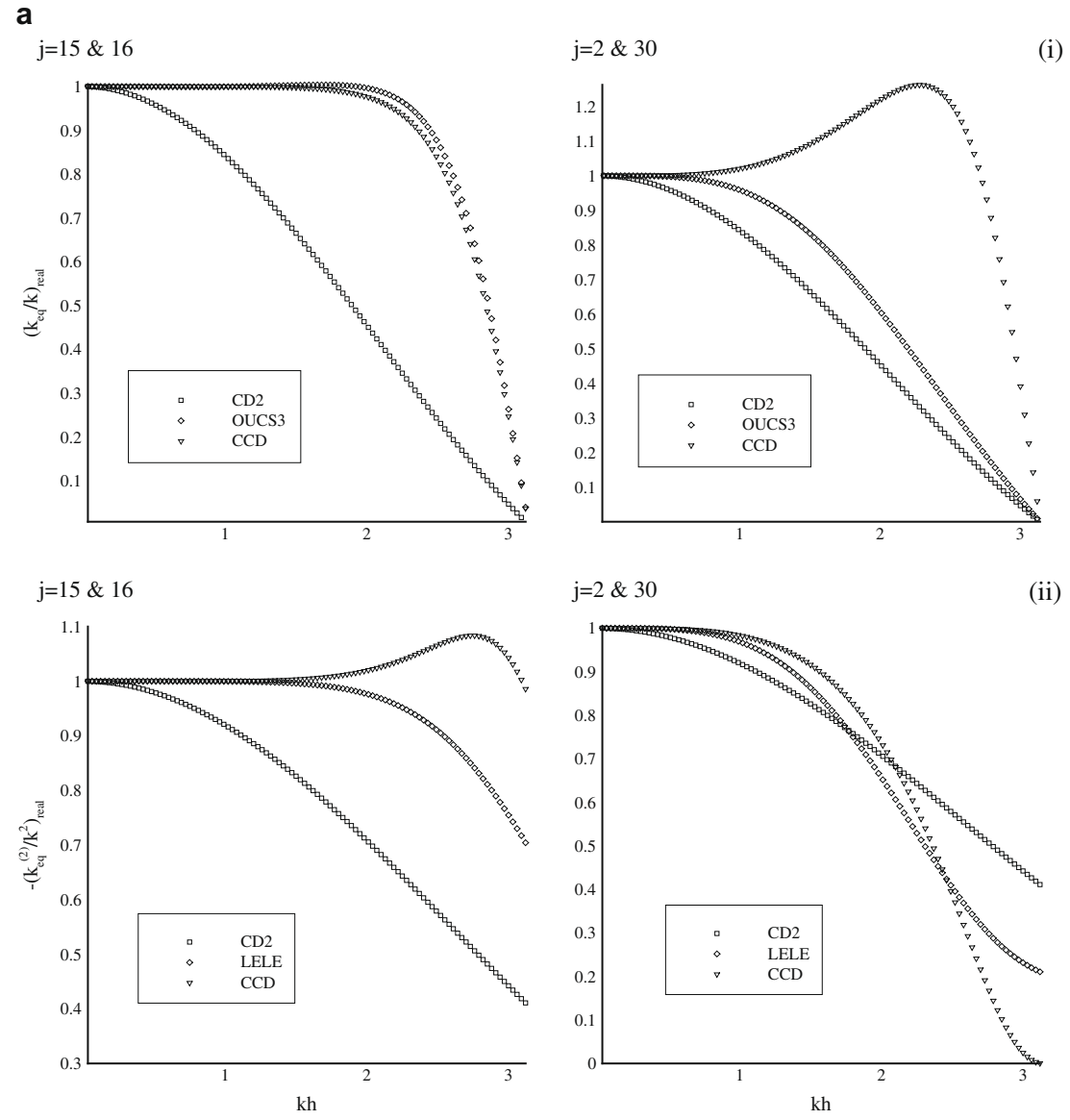

Fig. 1. (a) (i) Scale resolution given by real part of k_{eq}/k for first derivative and (ii) effectiveness of dissipation term representation given by the real part of $-k_{eq}^{(2)}/k^2$ are plotted against non-dimensional wave number. (b) (i) Dissipation as given by imag. part of k_{eq}/k for first derivative and (ii) dispersion as given by imag. part of $-k_{eq}^{(2)}/k^2$ for second derivative, plotted against non-dimensional wave number.

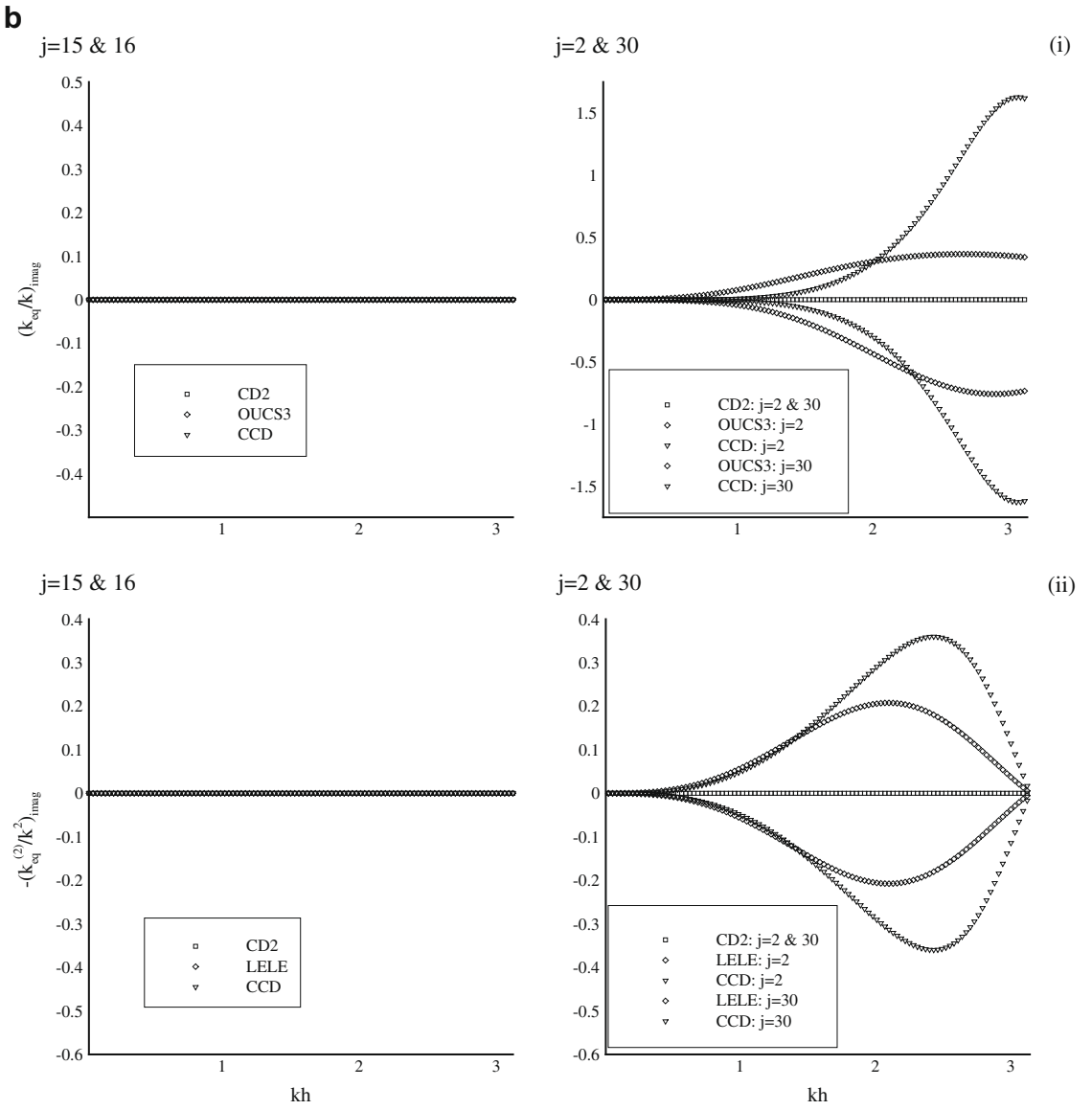

Fig. 1 *(continued)*

$$[u'_j]_{numerical} = \int ik_{eq} U e^{ikx_j}\, dk. \tag{9}$$

The quantity k_{eq}/k is in general complex, with real part represents the numerical method's ability to resolve different scales, while the imaginary part adds numerical dissipation, when it is negative. A similar procedure is adopted for the second derivative, with the real part of $k_{eq}^{(2)}/k^2$ represents the scale-wise dissipation term, while the imaginary part represents additional dispersion error.

We extend the full-domain Fourier–Laplace analysis of [3,5], with 31 points and compare the above quantities for the first and second derivatives in Fig. 1. In this figure, CCD is compared with an optimized compact difference scheme OUCS3 [3] and the explicit second order central difference scheme (CD_2) in the range ($0 \leqslant kh \leqslant \pi$). For the evaluation of second derivative, we have included the method due to Lele [1] that obtains this independently.

Fig. 1(a) shows the real part of k_{eq}/k and $-k_{eq}^{(2)}/k^2$ at interior and near-boundary nodes for the three schemes. The CCD [2] and the OUCS3 [3] schemes have resolution that is an order of magnitude higher than the CD_2 scheme for the first derivative. For near-boundary points ($j = 2$ and 30), CCD method shows overshoot of k_{eq}/k that can cause instability at high wave numbers. The second order accurate OUCS3 scheme shows better resolution for the first derivative, as compared to the formally sixth order accurate CCD scheme for the interior nodes. This is due to the fact that OUCS3 scheme is obtained by optimization of error in the k-space. The displayed $-k_{eq}^{(2)}/k^2$ of three methods have the compact difference scheme of Lele [1] that evaluates

second derivative directly. It is noted that unlike the first derivative, $-k_{eq}^{(2)}/k^2$ does not become zero at the Nyquist limit ($kh = \pi$) for the interior nodes. CCD method over-estimates second derivative at higher wave numbers and can be a source of error. However, up to $kh = 1.6$ the dissipation is represented exactly for the interior nodes. It is noted that for the near-boundary nodes at $j = 2$ and 30, CD_2 method provides better dissipation discretization property at high wave numbers as compared to the compact schemes. For the low wave numbers the compact schemes are far superior for all nodes. At intermediate wave numbers, CCD has better dissipation property as compared to Lele's scheme [1]. For internal flows, this feature of CCD may turn out to be useful, as we will show for the lid-driven cavity problem at high Reynolds numbers.

In Fig. 1(b), we show the imaginary part of k_{eq}/k and $-k_{eq}^{(2)}/k^2$ for the indicated methods. For the first derivative, this amounts to addition of numerical dissipation or *anti-diffusion* as shown in the frames indicated by (i) in the figure. For the interior nodes, as shown by the top left frame the methods are perfectly non-dissipative. However, for $j = 2$, both OUCS3 and CCD methods are unstable, while they are very dissipative at $j = 30$. For the second derivative, all the methods are extremely good for the interior nodes without adding any spurious dispersion, as shown in bottom left frame. However, both the CCD and Lele's scheme add spurious dispersion at the nea-boundary points with opposite features. There are no problems of spurious dispersion by CD_2 method.

Next, one would be interested in finding out the ability of these methods in producing accurate solutions for different types of partial differential equations that would require knowledge of numerical properties of these methods.

2.1. Other numerical properties of compact schemes

To investigate for the ability to obtain accurate solutions without error, we calibrate CCD and OUCS3 schemes by solving the 1D convection equation (1). To achieve high accuracy of the solution, we employ four-stage Runge–Kutta method for time-advancement. A brief description of the analysis method [5,14] to obtain essential numerical properties follows.

Numerically first derivative can be estimated as, $\{u'\} = \frac{1}{h}[C]\{u\}$. Using the spectral representation, this can also be alternatively written for the jth node as,

$$u'_j = \int \frac{1}{h} \sum_{l=1}^{N} C_{jl} U(k,t) e^{ik(x_l - x_j)} e^{ikx_j}\, dk. \tag{10}$$

The stability property for solving Eq. (1) is obtained from,

$$\frac{dU}{U} = -\left[\frac{cdt}{h}\right] \sum_{l=1}^{N} C_{jl} e^{ik(x_l - x_j)}. \tag{11}$$

On the left, dU represents variation of U when time is advanced by dt. The first factor on the right-hand side is the well-known CFL number (N_c). The nodal numerical amplification factor (G_j) was obtained for the four-stage Runge–Kutta time integration scheme in [14] as,

$$G_j = 1 - A_j + \frac{A_j^2}{2} - \frac{A_j^3}{6} + \frac{A_j^4}{24}, \tag{12}$$

where $A_j = N_c \sum_{l=1}^{N} C_{jl} e^{ik(x_l - x_j)}$.

If we represent the initial condition for Eq. (1) as

$$u(x_j, t=0) = u_j^0 = \int A_0(k) e^{ikx_j}\, dk, \tag{13}$$

then the general solution at any arbitrary time can be expressed as,

$$u_j^n = \int A_0(k) [|G_j|]^n e^{i(kx_j - n\beta_j)}\, dk, \tag{14}$$

where $|G_j| = (G_{rj}^2 + G_{ij}^2)^{1/2}$ and $tan(\beta_j) = -\frac{G_{ij}}{G_{rj}}$. Here, G_{rj} and G_{ij} are the real and imaginary parts of G_j, respectively. Thus, the phase of the solution is determined by $n\beta_j = kc_N t$, where c_N is the numerical phase speed, as defined in (15). This shows that the numerical phase speed is wave number dependent i.e. the numerical solution is dispersive, while the actual solution is non-dispersive.

The numerical dispersion relation is given by $\omega_N = c_N k$, instead of the physical dispersion relation, $\omega = ck$. The non-dimensional phase speed and group velocity at the jth discrete node can be expressed as [5,14],

$$\left[\frac{c_N}{c}\right]_j = \frac{\beta_j}{\omega \Delta t}, \tag{15}$$

$$\left[\frac{V_{gN}}{c}\right]_j = \frac{1}{hN_c} \frac{d\beta_j}{dk}. \tag{16}$$

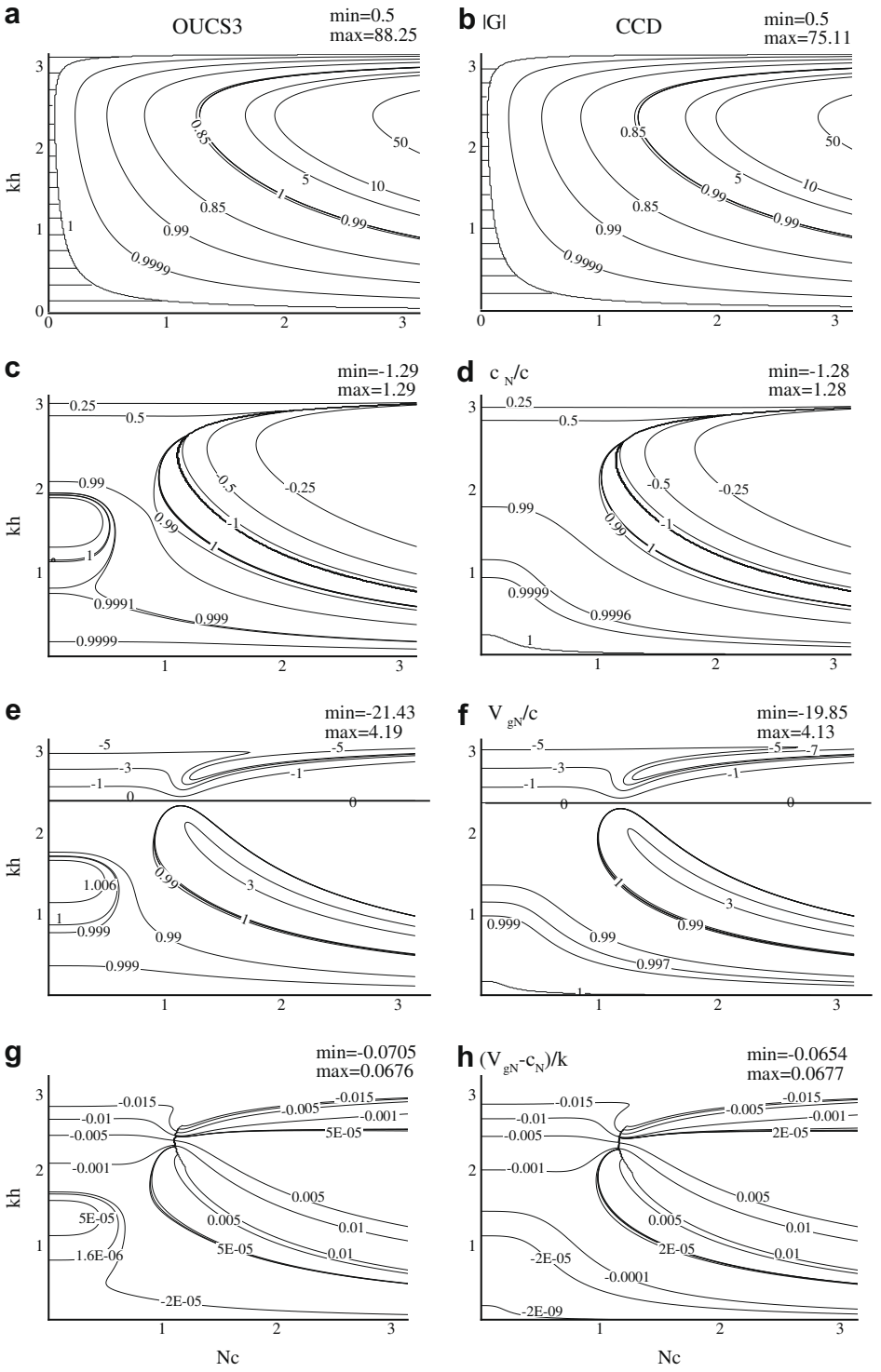

Fig. 2. Comparison of numerical properties for OUCS3 [3] and CCD [2] schemes, in determining error propagation as given in Eq. (3): (a and b) numerical amplification contours; (c and d) non-dimensional numerical phase speed contours; (e and f) non-dimensional numerical group velocity contours and (g and h) dispersion error term in Eq. (3), $(V_{gN} - c_N)/k$.

In Fig. 2, we have compared the properties of OUCS3 and CCD schemes in $(kh - N_c)$ plane for an interior node. The $|G|$ contours are shown in panels (a) and (b). One notes the hatched region (for small values of N_c), where both the methods are neutrally stable for the full range of kh – as desirable for DNS.

In the panels 2(c) and 2(d), the scaled numerical phase speed of the two methods are compared. From the first term on the right-hand side of Eq. (2), we note that the numerical phase speed will not cause error when c_N/c is identically one. For CCD, a region for small kh values exists where this error is absent. For OUCS3 method at very low values of N_c there is a small arc between $kh = 1$ and 2, where c_N/c is exactly equal to one. Such differences can be used to minimize error by appropriate choice of kh and N_c.

In panels (e) and (f) of Fig. 2, the scaled numerical group velocity contours are shown. Ideally, the ratio V_{gN}/c should be equal to one for solving Eq. (1). It is noted that for CCD this occurs for very small values of kh and N_c, while for OUCS3 it occurs inside a small arc around $kh = 1$. Thus, CCD has lower dispersion in comparison to OUCS3 scheme. We note from the second term on the right-hand side of Eq. (2), the integrand for the dispersion error depends on $(V_{gN} - c_N)/k$ and this quantity is shown in frames (g) and (h) of Fig. 2.

3. Solving wave propagation problems

Numerical properties of Fig. 2 determines the levels of error and a careful test is designed to solve Eq. (1). To obtain lower error, we have used a value of $N_c = 0.01$, so that neutral stability is ensured that makes the third term on the right-hand side of Eq. (2) identically equal to zero. To highlight the importance of phase and dispersion errors, the propagation of a discontinuous ramp function (shown in Fig. 3(a)) is considered that will excite a wide band of wave numbers due to slope discontinuities. The ramp angle considered is very small (36°) that makes the first term on the right-hand side of Eq. (2) unimportant. Larger ramp angles cause higher $\frac{\partial u_N}{\partial x}$, that magnifies phase error, giving rise to oscillations near discontinuities (Gibbs' phenomenon). From the plotted errors in Fig. 3(b) at $t = 0.01$, one notes the oscillations originating at the points of slope discontinuities at the foot and the shoulder of the ramp. These discontinuities are responsible for very high wave number components. In the following frame (at $t = 0.10$) one can identify the upstream propagating error-packets from the discontinuities for both the methods for wave number components with $kh > 2.5$. The panels (e) and (f) of Fig. 2, show that V_{gN}/c is negative for these methods. Thus, these error components (with $kh > 2.5$) travel in the upstream direction. The actual signal propagation speed for the case considered is $c = 1$. One notes the upstream propagating components traverse a distance of 4 by $t = 0.8$, with the leading packet arriving at the inflow for the OUCS3 scheme. For CCD scheme the arrival time is slightly lower. It can be explained why the maximum error for OUCS3 is lower than that for CCD scheme from the information contained in Fig. 3(c). For the present propagation problem, the dispersion error is contributed by the second term on the right-hand side of Eq. (2) for which the integrand consist of the term $(V_{gN} - c)/k$. For the OUCS3 method, $(V_{gN} - c)/k$ changes sign and there is cancellation of error at small wave numbers (shown in the inset of Fig. 3(c)). For the CCD method, this term is relatively high at medium to high wave number ranges, causing higher error.

Another important difference is noted when the upstream propagating error reaches the inflow of the domain. This relates to the numerical properties for the near-boundary points. Upon reflection, the upstream propagating error reflects as the complement of the incident wave ($(kh)_{reflected} = \pi - (kh)_{incident}$), as a low wave number downstream propagating wave. For the CCD method, such downstream propagating waves are unstable at $j = 2$ and 3 – as noted in Fig. 3(b) for $t = 0.8$, near the inflow. This gives rise to high magnitude error at the inflow for the CCD method. One does not see such error growth for the OUCS3 method. Such numerical instabilities noted for CCD is also accompanied by massive attenuation near the outflow. Both these problems of instability and attenuation, prompted us to develop an improved CCD scheme as given in the next subsection.

3.1. A new combined compact difference (NCCD) scheme

Ideas followed here are essentially the same that were used in [3,5] in developing a new compact scheme with no numerical instability near the inflow and excessive attenuation near the outflow. But before we discuss about stability, let us look at the resolution and added diffusion via the spatial discretization of first derivative alone. In Fig. 4(a), the real and the imaginary parts of k_{eq}/k are shown on the left column for the CCD scheme. The real part shows an overshoot for k_{eq}/k at $j = 2$ and 30, that can potentially lead to large error. The imaginary part of k_{eq}/k shown in the lower left frame of Fig. 4(a) shows that this is very high and positive-indicative of massive addition of *anti-diffusion* at $j = 2$ and 3. Because of the antisymmetric nature of Eqs. (7) and (8), as compared to Eqs. (5) and (6), we see massive added dissipation at $j = N$ and $N + 1$. One also notices zero imaginary part of k_{eq}/k for the interior nodes – due to perfectly central stencils of CCD, as given in Eqs. (3) and (4). Thus, CCD has good properties in the interior with problems near the boundaries.

In the proposed NCCD scheme, we replace the boundary closure schemes (Eqs. (5)–(8)) by the following explicit stencils for the nodes at $j = 2$ and N [23]:

$$f_2' = \frac{1}{h}\left[\left(\frac{2\beta_2}{3} - \frac{1}{3}\right)f_1 - \left(\frac{8\beta_2}{3} + \frac{1}{2}\right)f_2 + (4\beta_2 + 1)f_3 - \left(\frac{8\beta_2}{3} + \frac{1}{6}\right)f_4 + \frac{2\beta_2}{3}f_5\right], \tag{17}$$

$$f_N' = -\frac{1}{h}\left[\left(\frac{2\beta_N}{3} - \frac{1}{3}\right)f_{N+1} - \left(\frac{8\beta_N}{3} + \frac{1}{2}\right)f_N + (4\beta_N + 1)f_{N-1} - \left(\frac{8\beta_N}{3} + \frac{1}{6}\right)f_{N-2} + \frac{2\beta_N}{3}f_{N-3}\right], \tag{18}$$

$$f_2'' = (f_1 - 2f_2 + f_3)/h^2, \tag{19}$$

$$f_N'' = (f_{N+1} - 2f_N + f_{N-1})/h^2 \tag{20}$$

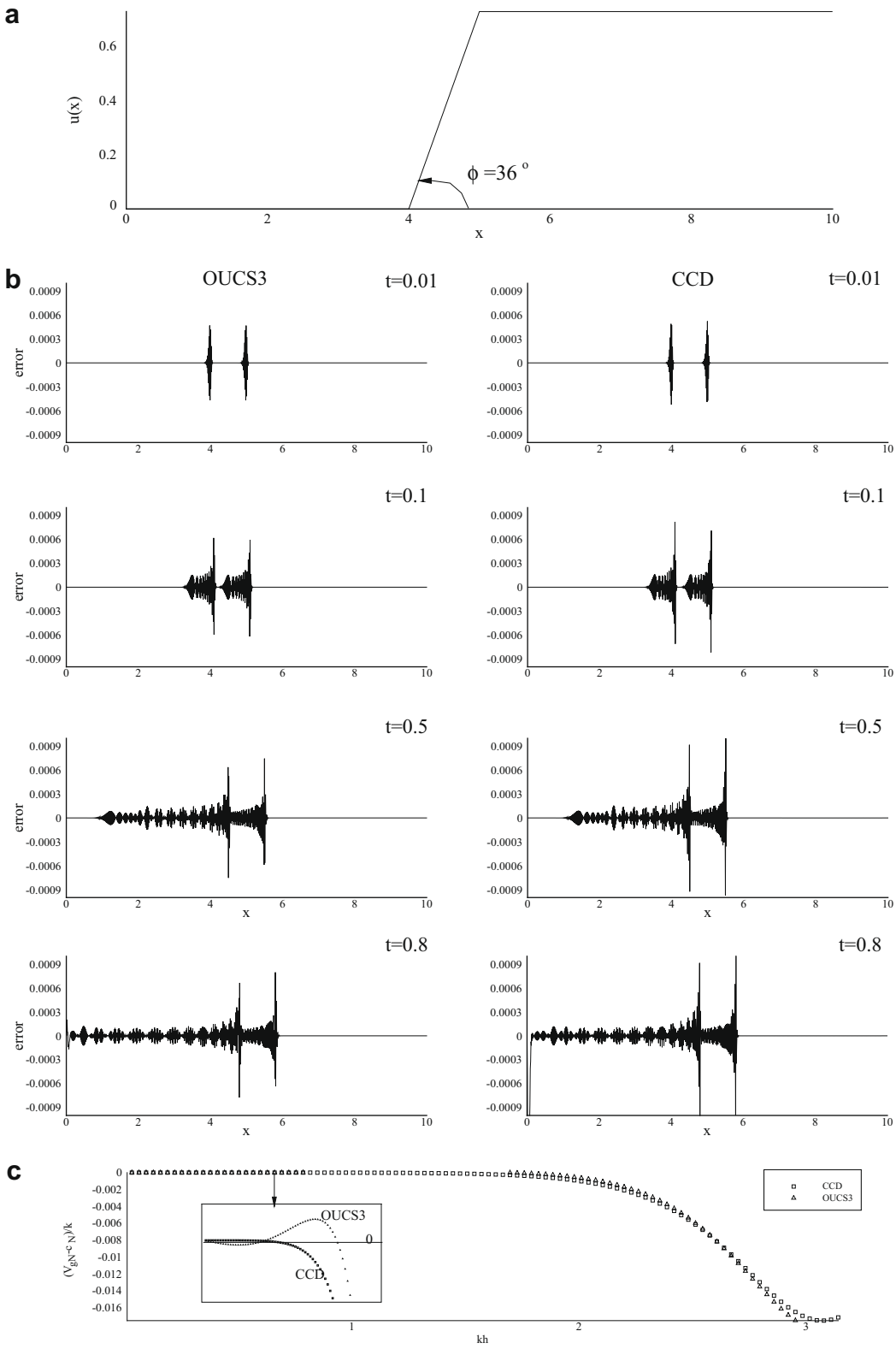

Fig. 3. Propagation of a ramp signal (a) following Eq. (1); (b) error evolution with time for OUCS3 [3] (left) and CCD [2] (right) schemes and (c) detailed variation of $(V_{gN} - c_N)/k$ vs k for these two methods.

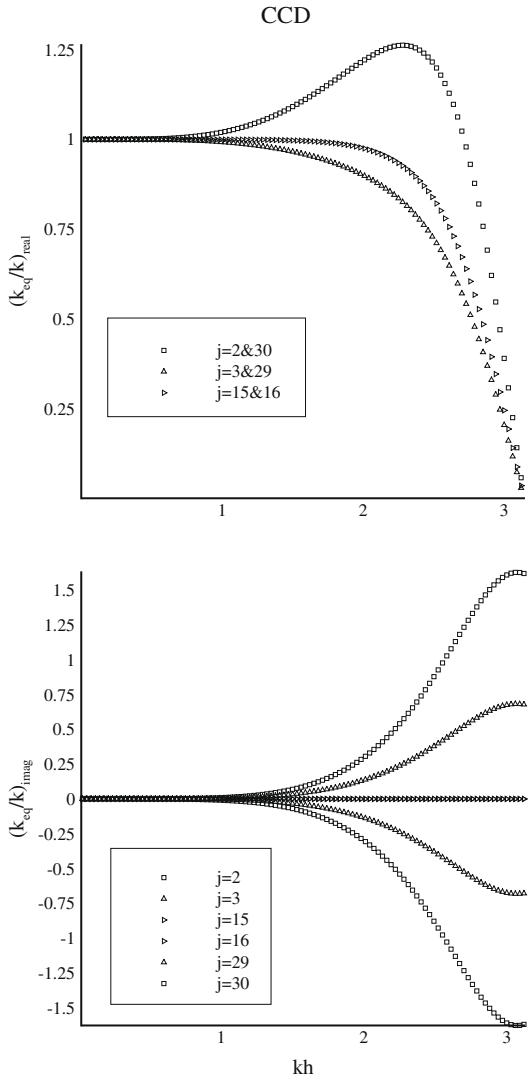

with $\beta_2 = -0.025$ and $\beta_N = 0.09$, as given in [23]. These values were optimized for the OUCS3 scheme and no efforts have been made to further change these for NCCD scheme. Because of these explicit stencils, we do not need any other stencils for $j = 1$ and $N + 1$, where one can directly apply the boundary conditions. For the interior points, we have used the same stencils given by Eqs. (3) and (4). Using the full-domain analysis method [3], we have obtained k_{eq}/k for different nodes and show them on the right column of Fig. 4(a). The real part of it shows no overshoot for either $j = 2$ and 30 or for $j = 3$ and 29 as compared to the CCD method. Interior nodes have the same properties for NCCD scheme, as obtained for the CCD scheme [2]. Major improvements are also seen for the imaginary part for NCCD scheme, with the values either zero or negative – except for the node $j = 2$. This node has *anti-diffusion* that is immediately followed by milder dissipation at $j = 3$. In a propagation problem, the instability at $j = 2$ will not be affecting the solution, because of the stabilizing influence of $j = 3$ followed by neutral stability at subsequent nodes. This was not the case with CCD, where numerical instabilities were very large and not followed by points with stabilizing influence. Additionally, one does not use the derivatives calculated by the compact scheme for $j = 2$, due to its unstable nature. After calculating the derivatives at all the nodes, the derivative at $j = 2$ is replaced by the non-dissipative, second order central scheme in all applications. One also notes the dissipative nature of NCCD is much lower as compared to CCD scheme near the outflow. In Chu and Fan [2], *anti-diffusion* near the inflow was not noticed because even in solving non-periodic problems, boundary closure was not used at all. Only

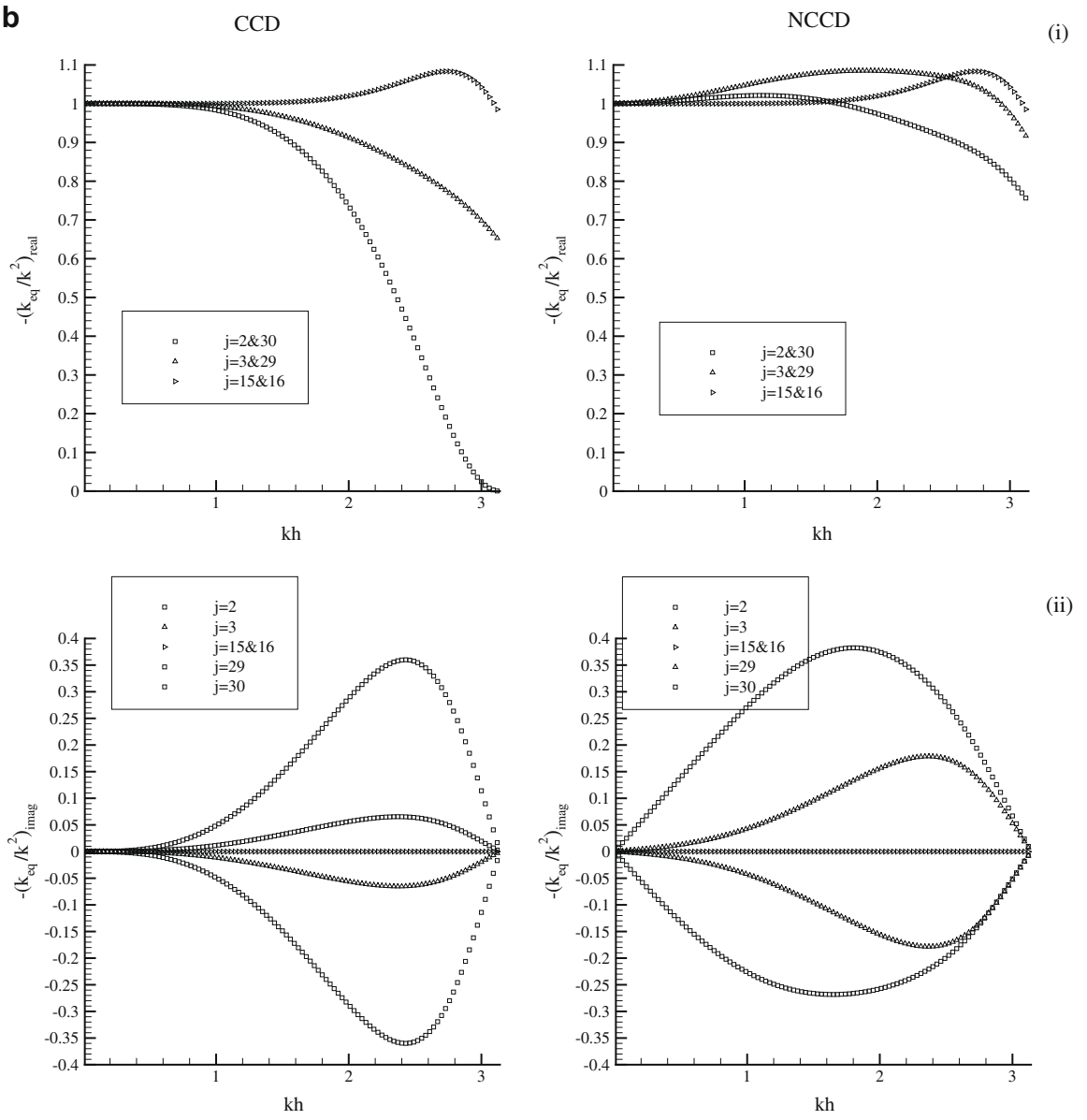

Fig. 4 (*continued*)

Eqs. (3) and (4) were used in addition to the finite difference equation. This was possible due to the Dirichlet conditions at the boundary.

We can write the NCCD stencils given by Eqs. (3), (4) and (17)–(20) as,

$$[A_1]\{u\}' + [B_1]\{u''\} = [C_1]\{u\},$$
$$[A_2]\{u'\} + [B_2]\{u''\} = [C_2]\{u\}.$$

On solving these two simultaneous equations we arrive at,

$$\{u'\} = \frac{1}{h}[D_1]\{u\},$$
$$\{u''\} = \frac{1}{h^2}[D_2]\{u\},$$

where

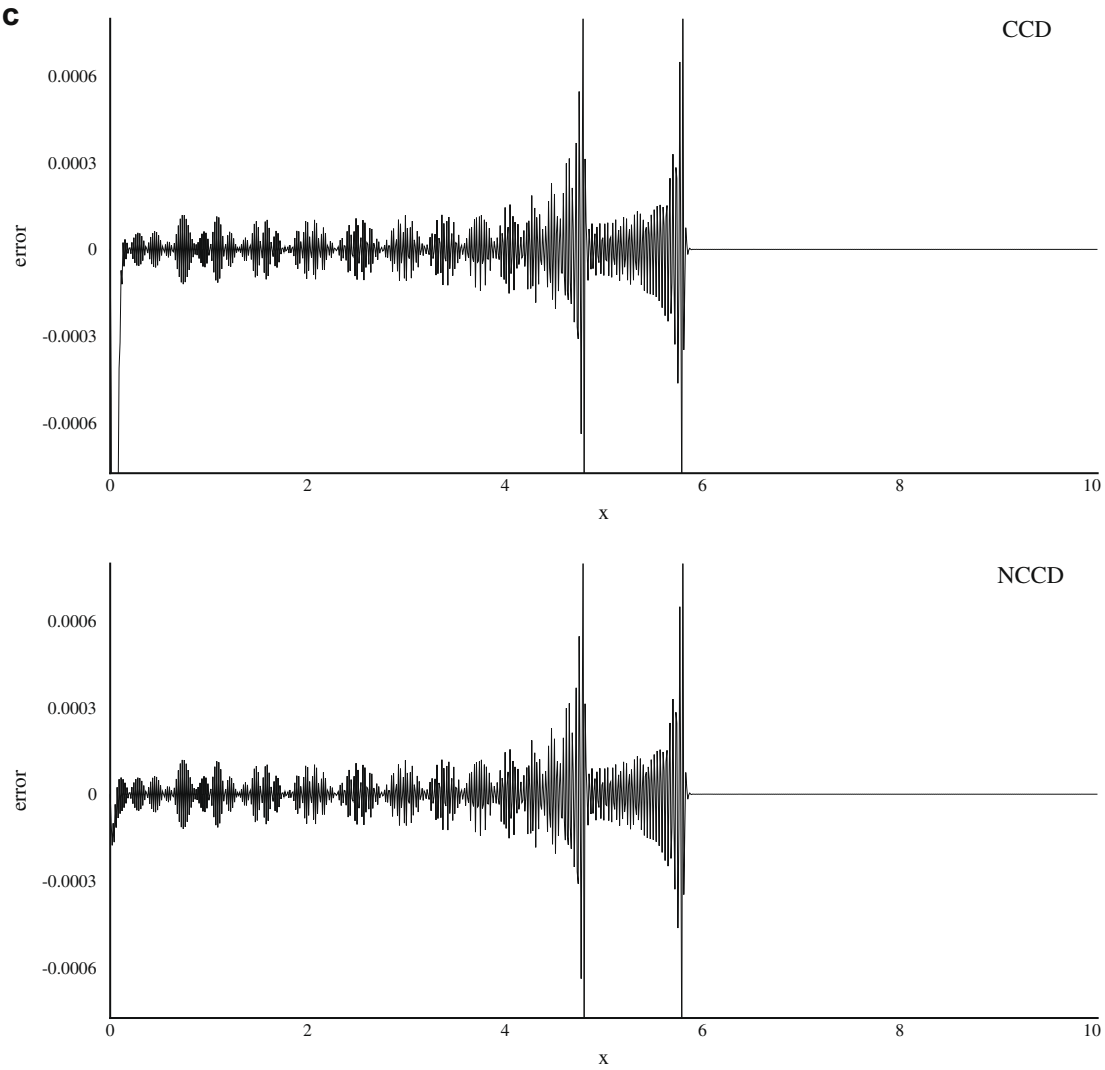

Fig. 4 (*continued*)

$$[D_1] = ([A_1] - [B_1][B_2]^{-1}[A_2])^{-1}([C_1] - [B_1][B_2]^{-1}[C_2]),$$
$$[D_2] = ([B_2] - [A_2][A_1]^{-1}[B_1])^{-1}([C_2] - [A_2][A_1]^{-1}[C_1]),$$

k_{eq}/k and $k_{eq}^{(2)}/k^2$ for first and second derivatives are evaluated using,

$$(k_{eq}/k)_j = \frac{1}{kh}\sum_{l=1}^{N+1}[D_1]_{jl}P_{lj},$$
$$(k_{eq}^{(2)}/k^2)_j = \frac{-1}{(kh)^2}\sum_{l=1}^{N+1}[D_2]_{jl}P_{lj},$$

where j defines the node number and

$$P_{lj} = e^{i(l-j)kh}.$$

The effectiveness of dissipation discretization by CCD and NCCD schemes have been compared in Fig. 4(b). There appears to be no difference between the two methods for the interior nodes. However, the noted problem of lack of dissipation at higher wave numbers for the near-boundary points for the CCD scheme has been removed significantly by the NCCD scheme. Although, the dispersion effects for the NCCD scheme has become worse.

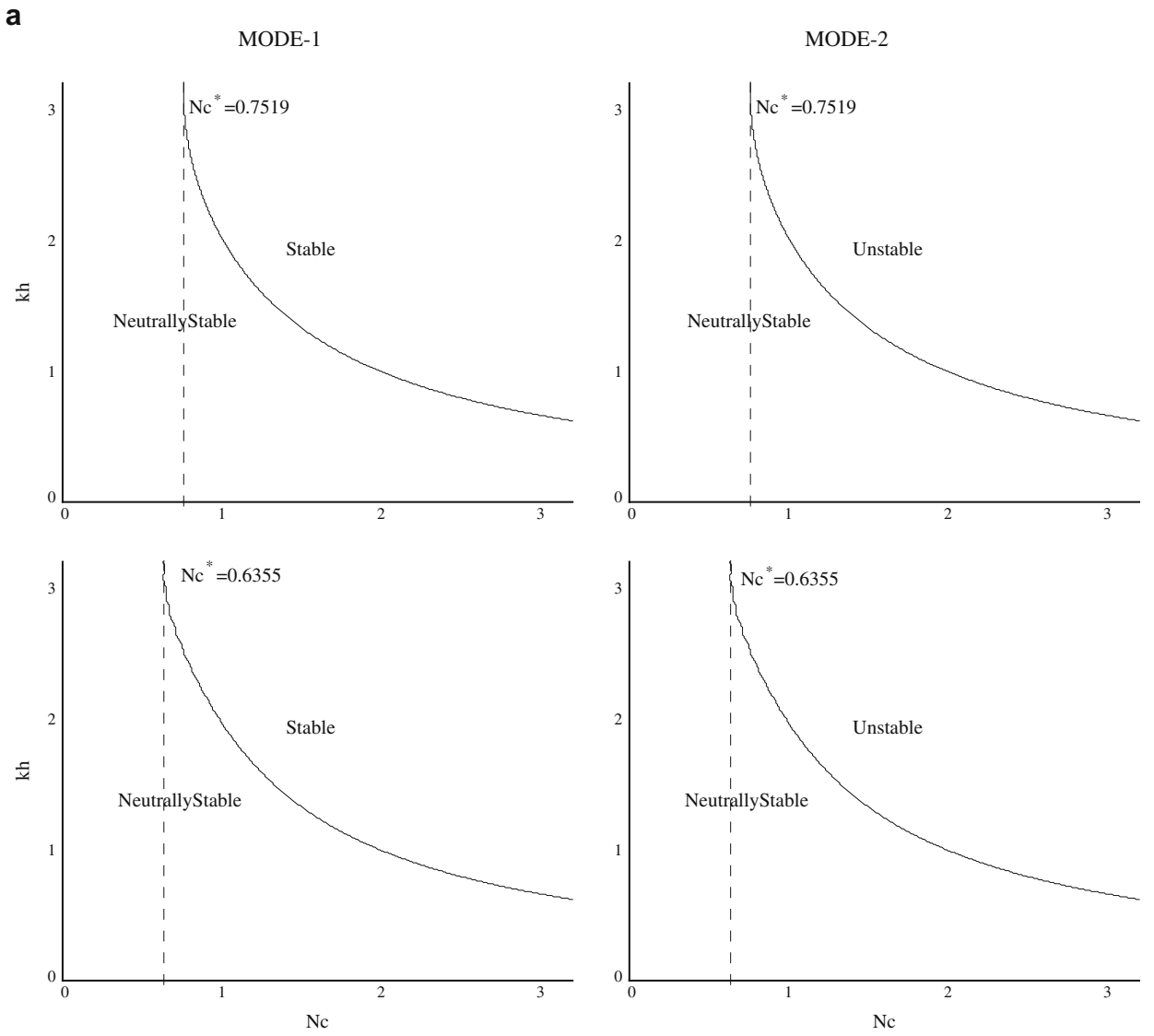

Fig. 5. (a) Neutral $|G|$ contour for Lele's scheme [1] (top) and NCCD (bottom) for solving Eq. (21). Critical CFL number (Nc^*) identified for both the modes of these methods. (b) Solution of Eq. (21) for the propagation of a wave packet by NCCD scheme (right) and Lele's scheme (left) [1].

In Fig. 4(c), the numerical solution of Eq. (1) is compared between CCD and NCCD schemes at $t = 0.8$. In the bottom panel, the results for NCCD scheme shows a small reflection of the error-packet, similar to that noted for OUCS3 scheme. This error is few orders of magnitude smaller as compared to that seen for CCD scheme shown in the top panel.

Next, we find out the efficacy of NCCD in evaluating second derivatives. This is done here by solving bi-directional wave equation and comparing the solution with the results obtained using the compact scheme due to Lele [1] that evaluates second derivative separately. The bi-directional wave equation solved here is given by,

$$\frac{\partial^2 u}{\partial t^2} - c^2 \frac{\partial^2 u}{\partial x^2} = 0. \tag{21}$$

Lele's scheme for second derivative [1] was also compared with the SOUCS3 scheme in [24] – a symmetrized version of the OUCS3 scheme, for solving Eq. (21). Here, we compare the numerical stability property of NCCD scheme with Lele's scheme [1] first and then we will compare the computed solution of (21). In Fig. 5(a), $|G|$-contours for these two schemes are shown demarcating the stable and unstable regions in the $(kh - N_c)$-plane, when the time derivative is discretized by leapfrog scheme. Because of the usage of the three-time level method one would have two modes of the numerical solution for which the region outside the curve (towards the origin) is neutrally stable for both the modes. The region inside the curve is stable for the Mode-1 and is unstable for the Mode-2. This is true for both NCCD and Lele's scheme. These figures also identify a

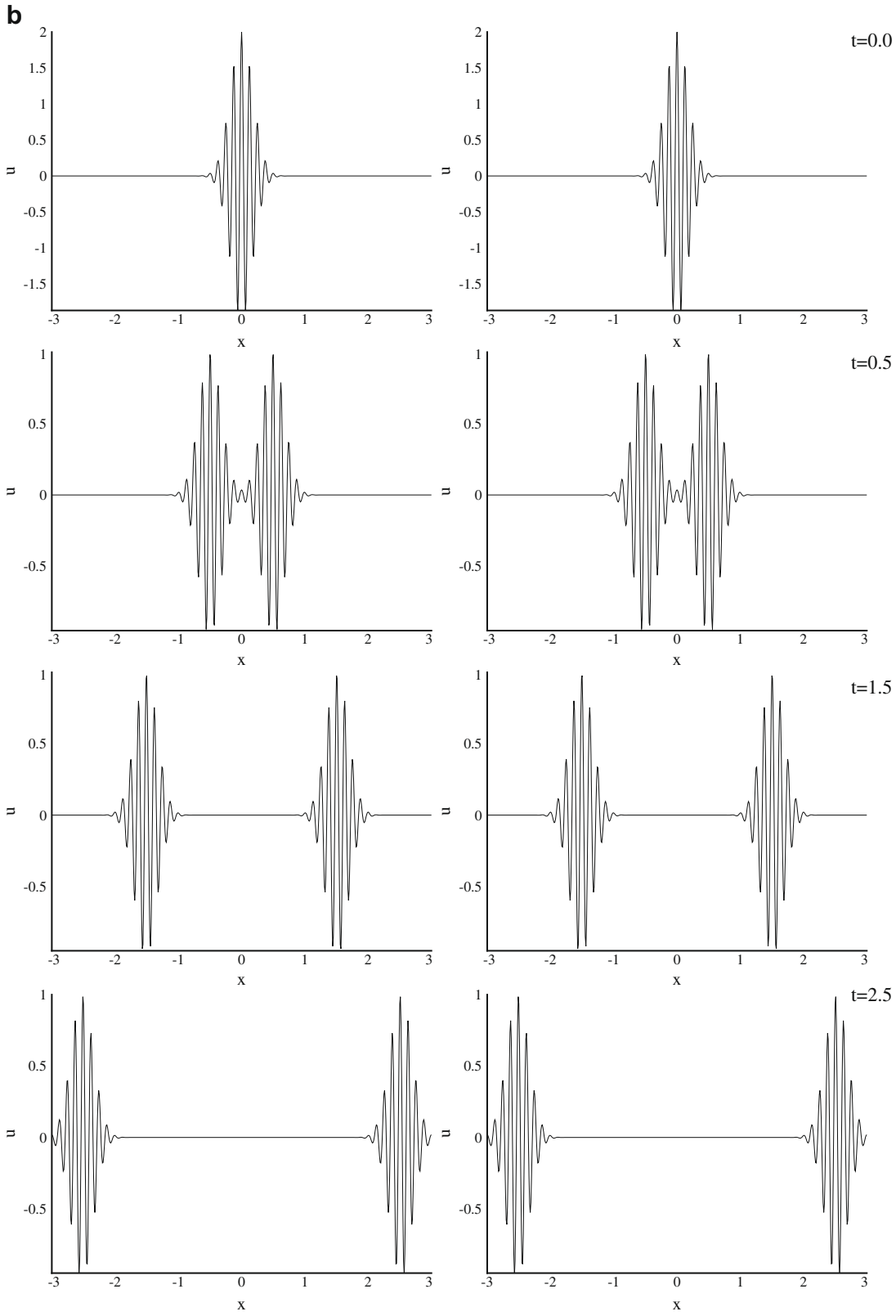

Fig. 5 (*continued*)

critical CFL number, below which the methods are perfectly neutrally stable. It is noted that for Lele's scheme, this is higher at $N_c^* = 0.7519$, as compared to $N_c^* = 0.6355$ for NCCD scheme. It was noted that for the symmetrized SOUCS3 scheme [24], $N_c^* = 0.8736$ was higher and the same could be done for NCCD scheme as well.

Both the schemes have been used to solve Eq. (21) for $c = 1$ with the initial condition given by, $u(x, t = 0) = 2e^{-16x^2} cosk_0 x$, with $k_0 = 50$, in a domain $-3 \leqslant x \leqslant 3$ with 601 equi-spaced points. The time step chosen was $\Delta t = 0.005$, so that $N_c = 0.5$. The computed solutions are shown in Fig. 5(b) at selected time instants and these two methods produce identical results. We furthermore note both the methods suffer no problems when the signal reflects from the boundaries, as noted from the solution at $t = 2.5$. However, with the CCD scheme, we would have large error when the signal reflects at the boundaries.

4. Solving the Stommel Ocean model problem

This problem was solved in [2] to establish the superiority of CCD over standard second order central difference scheme. The model problem involves solving the following equation given in Cartesian coordinates–ordinates as,

$$\left[\frac{\partial^2}{\partial x^2} + \frac{\partial^2}{\partial y^2}\right]\psi + \alpha\frac{\partial \psi}{\partial x} = -\gamma sin\left(\frac{\pi}{b}y\right). \tag{22}$$

Here x and y are the longitudinal and latitudinal coordinates–ordinates in the range $0 \leqslant x \leqslant \lambda$ and $0 \leqslant y \leqslant b$ for an Ocean at rest with depth D, that is set in motion by surface wind stress given by $-Fcos(\pi y/b)$. The latitudinal variation of the Coriolis parameter f is defined by $\beta = df/dy$, that is used in the model equation (22), with $\alpha = D\beta/R$ and $\gamma = F\pi/Rb$, where R is the frictional coefficient. The analytical solution of (22) is given by [2],

$$\psi = -\gamma\left(\frac{b}{\pi}\right)^2 sin\left(\frac{\pi y}{b}\right)(pe^{A_1 x} + (1-p)e^{A_2 x} - 1), \tag{23}$$

where $A_{1,2} = -\frac{\alpha}{2} \pm \sqrt{\frac{\alpha^2}{4} + \frac{\pi^2}{b^2}}$ and $p = (1 - e^{A_2\lambda})/(e^{A_1\lambda} - e^{A_2\lambda})$.

To solve Eq. (22) by NCCD, we have chosen the same parameters used in [2] and they are: $\lambda = 10^7$ m;$b = 2\pi \times 10^6$ m;$D = 200$ m;$F = 0.3 \times 10^{-7}$ m^2 s^{-2} and $R = 0.6 \times 10^{-3}$ m s^{-1}. We will show a results for $\beta = 10^{-11}$ m^{-1} s^{-1}, as also was given in [2].

In Chu and Fan [2], Eq. (22) was solved by using ADI method with Dirichlet condition on the boundary. In the first half-step of ADI, $\psi, \partial\psi/\partial x$ and $\partial^2\psi/\partial x^2$ are treated as unknowns at the $(N-1)$ interior points. Rest of the derivatives are treated as knowns, obtained from the usage of Eqs. (3) and (4) and the finite difference equation. This closes the system without the need to use boundary closure schemes of Eqs. (5)–(8). In the next half-step of ADI also, the boundary closure schemes were not used. In contrast to this approach, we have used the Bi-CGSTAB algorithm of [25] as applied to the linear system arising from discretization, while treating the function and its derivatives as unknowns. The derivatives have been obtained up front with the help of Eqs. (3),(4) and (17)–(20). Thus, the boundary closure schemes are in-built while evaluating the derivatives in the present method. As the exact solution is available, it is easy to monitor the convergence of the computed solution, as performed in [2]. However, we have followed the often-practiced strategy of tracking the convergence by evaluating the

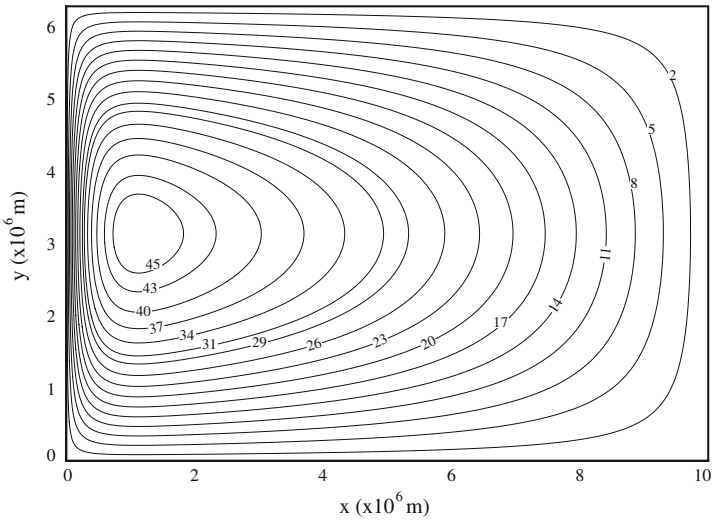

Fig. 6. Computed solution for Stommel Ocean model with $\beta = 10^{-11}$ using NCCD scheme with (201×201) grid. Exact [2] and computed solutions are indistinguishable here.

Table 1
Convergence history and the error obtained in solving Stommel Ocean model ($\beta = 10^{-11}$) for different grids using NCCD.

Grid size	Error	CPU time (s)	Number of iterations
9×9	1.020×10^{-8}	< 1	27
10×10	1.940×10^{-8}	< 1	24
14×14	6.433×10^{-9}	< 1	27
20×20	1.164×10^{-9}	< 1	43
30×30	1.073×10^{-9}	< 1	67
50×50	6.946×10^{-9}	1.2	122
100×100	2.217×10^{-9}	5.1	264
151×151	2.279×10^{-9}	40.5	424
201×201	5.490×10^{-10}	180.0	575

Table 2
Maximum and minimum values of stream function computed by different methods for $Re = 1000$.

S. No	Methods and grids	ψ_{max}	ψ_{min}
1	Botella and Peyret [27] ($N = 160$)	0.1189366	-1.729717×10^{-3}
2	Ghia et al. [26] (129×129)	0.117929	-1.75102×10^{-3}
3	Bruneau and Saad [28] (129×129)	0.11786	-1.7003×10^{-3}
4	Present work (129×129)	0.118561	-1.71902×10^{-3}
5	Present work (150×150)	0.118714	-1.72181×10^{-3}
6	Present work (180×180)	0.118821	-1.72269×10^{-3}
7	Present work (210×210)	0.118873	-1.72434×10^{-3}
8	Present work (257×257)	0.118908	-1.72577×10^{-3}
9	Bruneau and Saad [28] (1024×1024)	0.11892	-1.7292×10^{-3}

solution residue at each point of the domain (R_{ij}), defined below. We have used the residue per point as the convergence criterion here. The residue is obtained from,

$$R_{ij} = \left[\nabla^2\psi + \alpha\frac{\partial\psi}{\partial x} + \gamma sin\left(\frac{\pi y}{b}\right)\right]_{ij}. \tag{24}$$

We have solved the problem using a uniform grid. In Fig. 6, the computed and exact solution appear together and are indistinguishable. The convergence history of the solution is shown for different grid size in Table 2. One notices the residue to converge up to eighth to tenth decimal places. Even for the coarsest grid, one obtains eight digit accuracy in a fraction of a second. One interesting aspect of convergence history is that the average residue improves with grid refinement up to the grid of size (30×30) and further grid refinement shows increased residue abruptly. Similar reduction in residue was also recorded in [2] up to a grid of size (27×27). However, further refined grid solution was not presented in [2]. In the present exercise, when solution was obtained with further refined grid, we notice a local minimum for the (30×30) grid. However, when the grid size was progressively refined to (201×201), we again obtained very accurate solution, with residue decaying to tenth decimal place.

5. Solving the 2D lid-driven cavity problem

The flow inside a lid-driven cavity constitutes a classical benchmark problem, due to its unique boundary conditions that allow comparing any new method's potential for solving Navier–Stokes equation for internal flows. While there are many papers on this topic, here we refer to the oft quoted results in Ghia et al. [26] and Botella and Peyret [27] to compare our results obtained using NCCD. We also refer to Bruneau and Saad [28] and Pandit et al. [29] those reporting accurate results for the same problem. While in [28] the first Hopf bifurcation is identified via a study of the linearized problem, Pandit et al. [29] reports the results by using a fourth order compact scheme. Of course, the results in [26,27] are still considered as accurate results for the lower Reynolds numbers. Of specific interest is the results of Botella and Peyret [27] who provided the highly accurate solution to the problem using Chebyshev collocation spectral method. We would refer to their results for $Re = 1000$ with $N = 160$ terms Chebyshev polynomial representation.

Here the two-dimensional viscous flow as governed by the Navier–Stokes equation is solved in stream function – vorticity formulation given in non-dimensional form by,

$$\nabla^2\psi = -\omega, \tag{25}$$

$$\frac{\partial\omega}{\partial t} + V\cdot\nabla\omega = \frac{1}{Re}\nabla^2\omega, \tag{26}$$

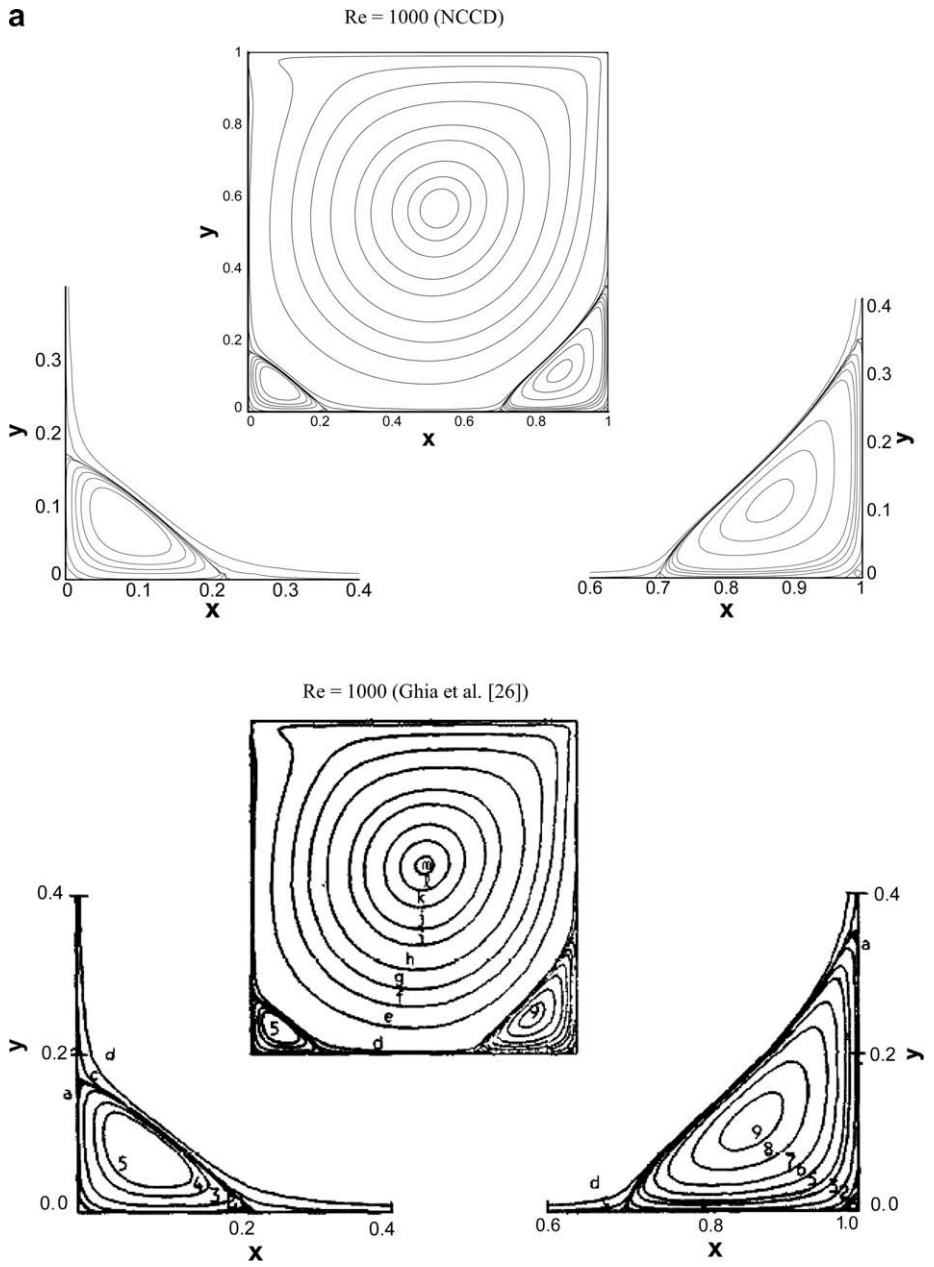

Fig. 7. (a) Stream function contours for lid-driven cavity problem with $Re = 1000$ and (129×129) grid using NCCD scheme (top) compared with the computations of Ghia et al. [26] (bottom). (b) Vorticity contours for lid-driven cavity problem with $Re = 1000$ and (129×129) grid using NCCD scheme (top) compared with the computations of Ghia et al. [26] (bottom). (c) Comparison of u-velocity along the vertical centerline of the lid-driven cavity for NCCD scheme with (129×129) grid and computations of Ghia et al. [26] with (129×129) grid for $Re = 1000$. (d) Comparison of v-velocity along the horizontal centerline of the lid-driven cavity for NCCD scheme with (129×129) grid and computations of Ghia et al. [26] with (129×129) grid for $Re = 1000$.

where ω is the out of plane component of vorticity and the velocity is related to the stream function by $V = \nabla \times \vec{\psi}$, where $\vec{\psi} = (0, 0, \psi)$. The ψ–ω formulation is preferred here due to its inherent accuracy and computational efficiency in satisfying mass conservation exactly everywhere. We have used the sides of the square cavity as the length scale and the constant velocity with which the top lid is driven from left to right, as the velocity scale. The time scale is derived from these two scales. As we intend to use NCCD scheme for solving Eqs. (24) and (25), we will use a uniform grid so that the Laplacian operators can be expressed in terms of pure second derivatives.

In Fig. 7, we show the results for the case of Re = 1000, alongside similar results reported in [26] using identical uniform grids. These results are obtained using a (129×129) grid, with first and second derivatives obtained by NCCD scheme in

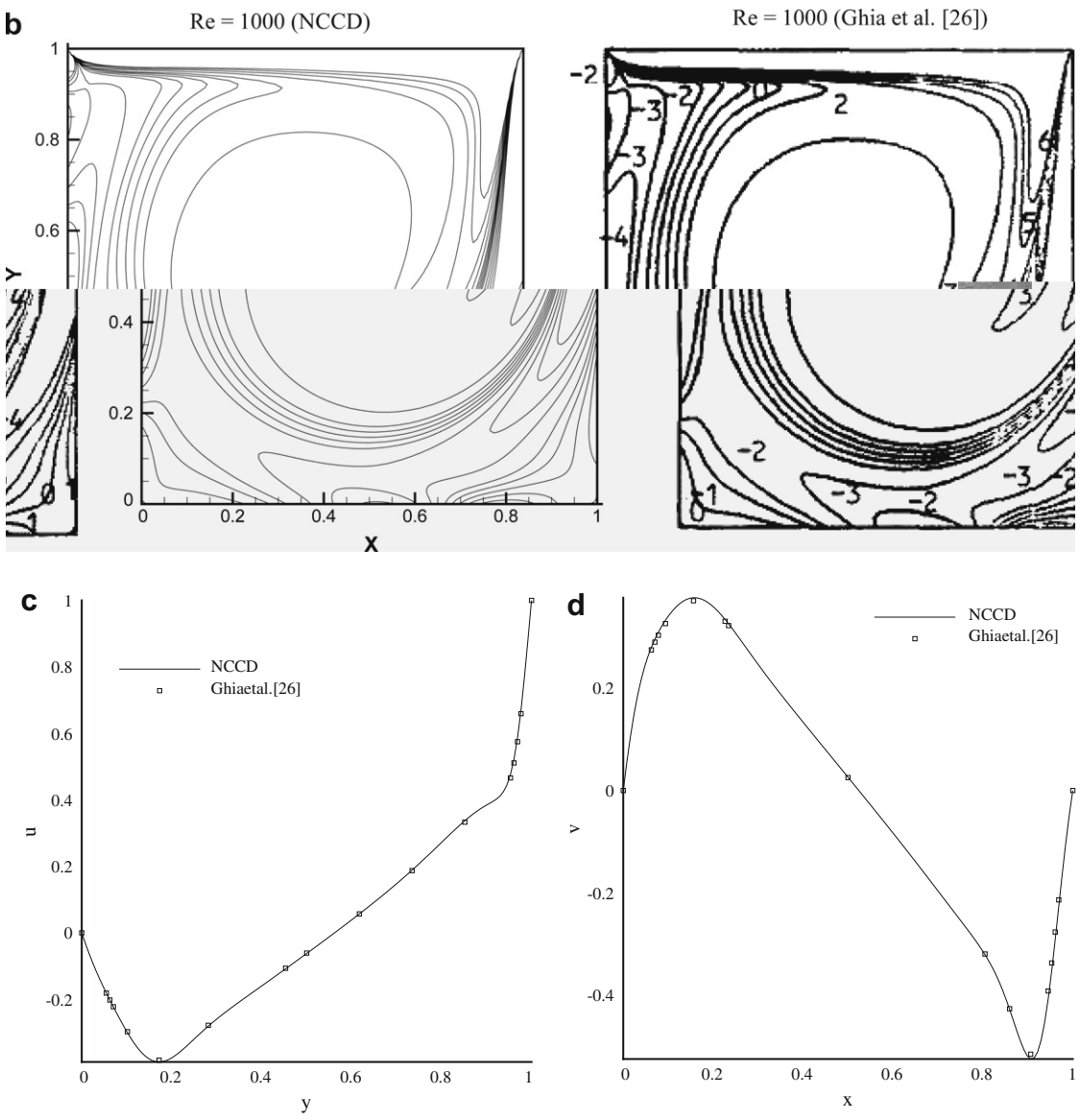

Fig. 7 (*continued*)

solving both the stream function equation (SFE) and vorticity transport equation (VTE). We have used the Bi-CGSTAB method of [25] in solving the SFE. The VTE is solved using four-stage Runge–Kutta time discretization and the NCCD for spatial discretization. The solution is advanced in time till the time derivative of ω is reduced to 10^{-10} for $Re \leqslant 3200$ i.e. we have truly steady state results for the results shown in Figs. 7 and 8. However, for the case of $Re = 10,000$, we show multi-periodic solution in Figs. 9 and 10. In Fig. 9, we compare the results obtained using NCCD and Lele's scheme for the evaluation of various derivatives. In Fig. 10, the results obtained by NCCD method will be compared with the very fine grid calculations of [28].

In Fig. 7(a), our computed solutions shown in top are compared with the results of [26] in the bottom. It is clearly evident that there is excellent qualitative match between the two sets of results. The primary and secondary vortices are captured identically by the present method as compared to that in [26]. In Fig. 7(b), the computed vorticity contours are compared between the present computations with that given in [26]. Quantitative comparison between the present and the computed results from [26] are provided in Fig. 7(c) and (d). In Fig. 7(c), the x-component of velocity along the vertical centerline is plotted and this shows perfect match between the present results with that from [26]. The y-component of velocity along the horizontal centerline is plotted in Fig. 7(d) and one can once again note perfect match between the present computation with that reported in [26]. Further quantitative match between present computations with other benchmark results will be provided in Table 2.

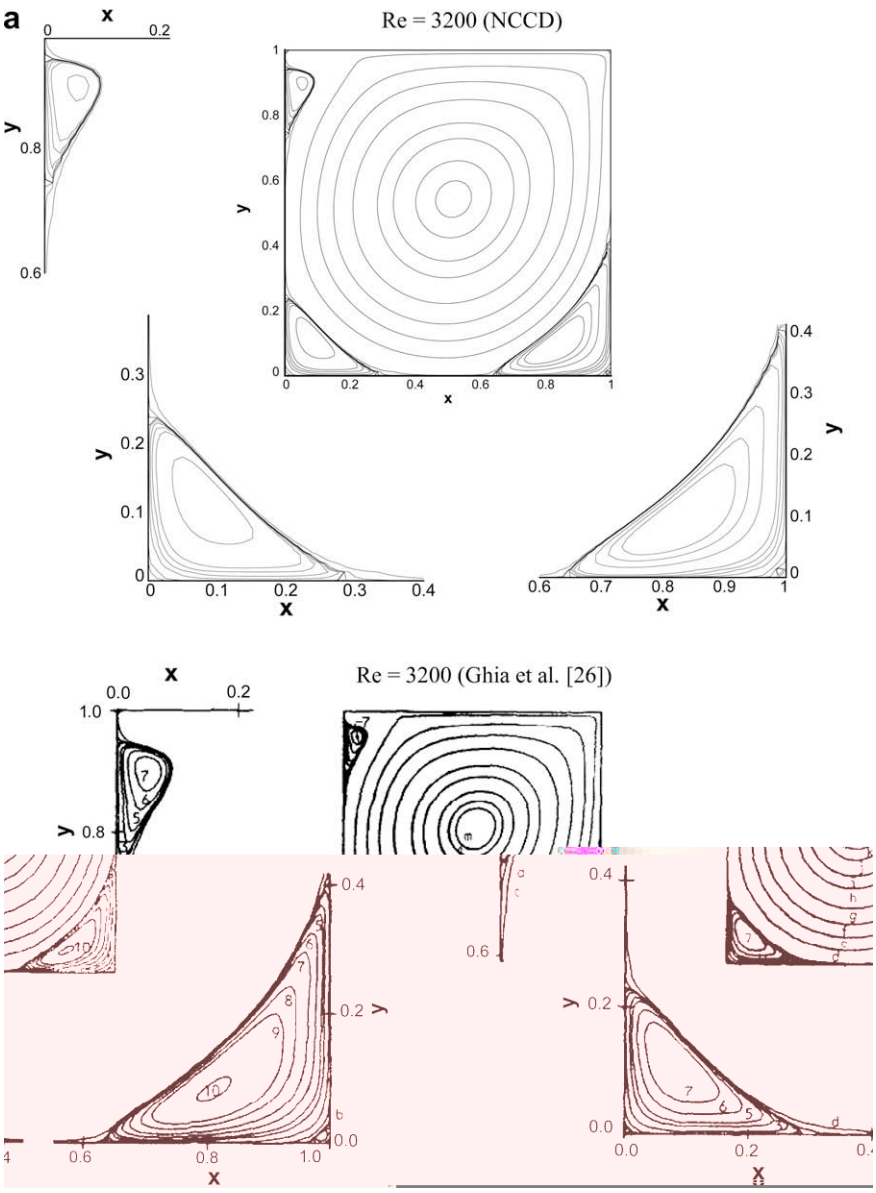

Fig. 8. (a) Stream function contours for lid-driven cavity problem with $Re = 3200$ using NCCD scheme with (81×81) grid (top) compared with the computations of Ghia et al. [26] with (129×129) grid (bottom). (b) Voricity contours for lid-driven cavity problem with $Re = 3200$ using NCCD scheme with (81×81) grid (top) compared with the computations of Ghia et al. [26] with (129×129) grid (bottom). (c) Comparison of u-velocity along the vertical centerline of the lid-driven cavity for NCCD scheme with (81×81) grid and computations of Ghia et al. [26] with (129×129) grid for $Re = 3200$. (d) Comparison of v-velocity along the horizontal centerline of the lid-driven cavity for NCCD scheme with (81×81) grid and computations of Ghia et al. [26] with (129×129) grid for $Re = 3200$.

In Fig. 8, we have similarly compared our results using a grid of (81×81) with that from Ghia et al. [26] who used a (129×129) grid for $Re = 3200$. In Fig. 8(a) and (b), stream function and vorticity contours are plotted, respectively and compared with that in [26]. Present computations are shown on the top, while the results from [26] are shown at the bottom. Once again one notes excellent qualitative match between the two sets of results. The corresponding quantitative comparison between the two computations are shown in Fig. 8(c) and (d). In Fig. 8(c), the x-component of velocity along the vertical centerline is shown plotted and in Fig. 8(d), the y-component of velocity along the horizontal centerline is compared between the two sets of computations. Despite the fact that far fewer points are taken for the present set of computation, the agreement between the two is note-worthy.

To obtain a sense of absolute accuracy of different methods for this flow field, we have performed many calculations for $Re = 1000$ using different grids. The maximum and minimum values of the computed stream function in the domain by the

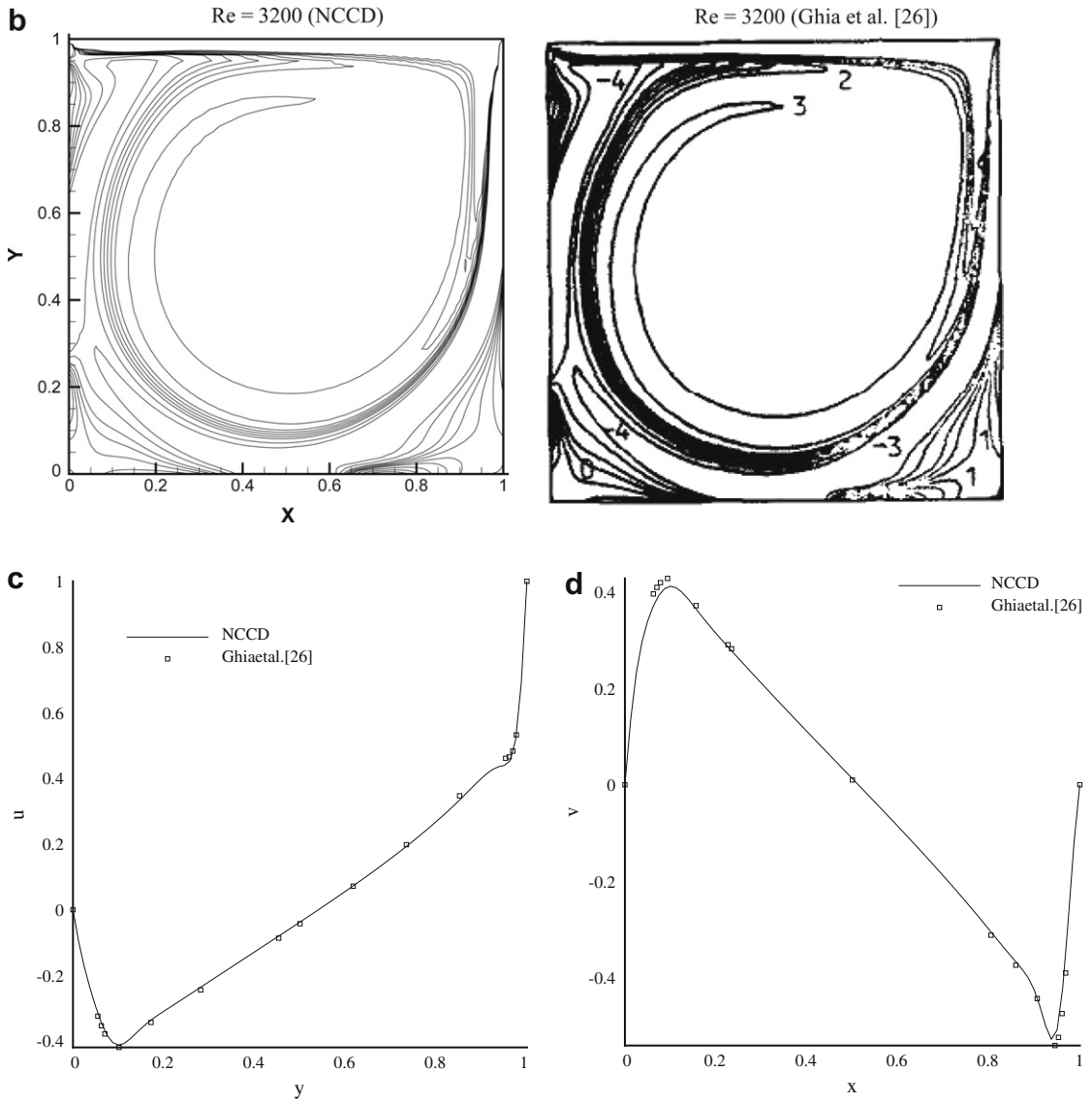

Fig. 8 (*continued*)

present method is compared with other benchmark results in Table 2. The spectral collocation results of Botella and Peyret [27] using 160 terms Chebyshev polynomial representation to be the most accurate one for $Re = 1000$ and is used as a benchmark for this flow field.

The results in [27] are the most accurate and one notes that the results of [26] match only up to second significant digits with that in [27]. The method used in [26] is a low order method; the results suffer from the implicit filtering associated with the multi-grid method used to solve SFE. We specifically note that in discretizing convection terms in [26], first order upwinding was used that adds a large amount of numerical dissipation interfering with the physical dissipation of the problem. How various discretization schemes affect final results can be viewed by comparing the results of [28] with that in [26,27]. In Bruneau and Saad [28], the time discretization was performed by second order Gear method and the spatial discretization is a blend of a second and a third order accurate schemes. The methods of discretization in [28] do not yield results more accurate than that in [26,27], when (129×129) grid was used. To obtain good results as compared to [27], a much refined (1024×1024) grid was needed in [28] to match up to four significant digits. The spectral collocation method [27] is a global method, that provides the maximum and minimum values of ψ without depending on the grid point location. The results obtained by other methods of Table 2, depend on the location of the nearest point in the neighborhood of the maximum and minimum points. This is evident when one notes the finer grid

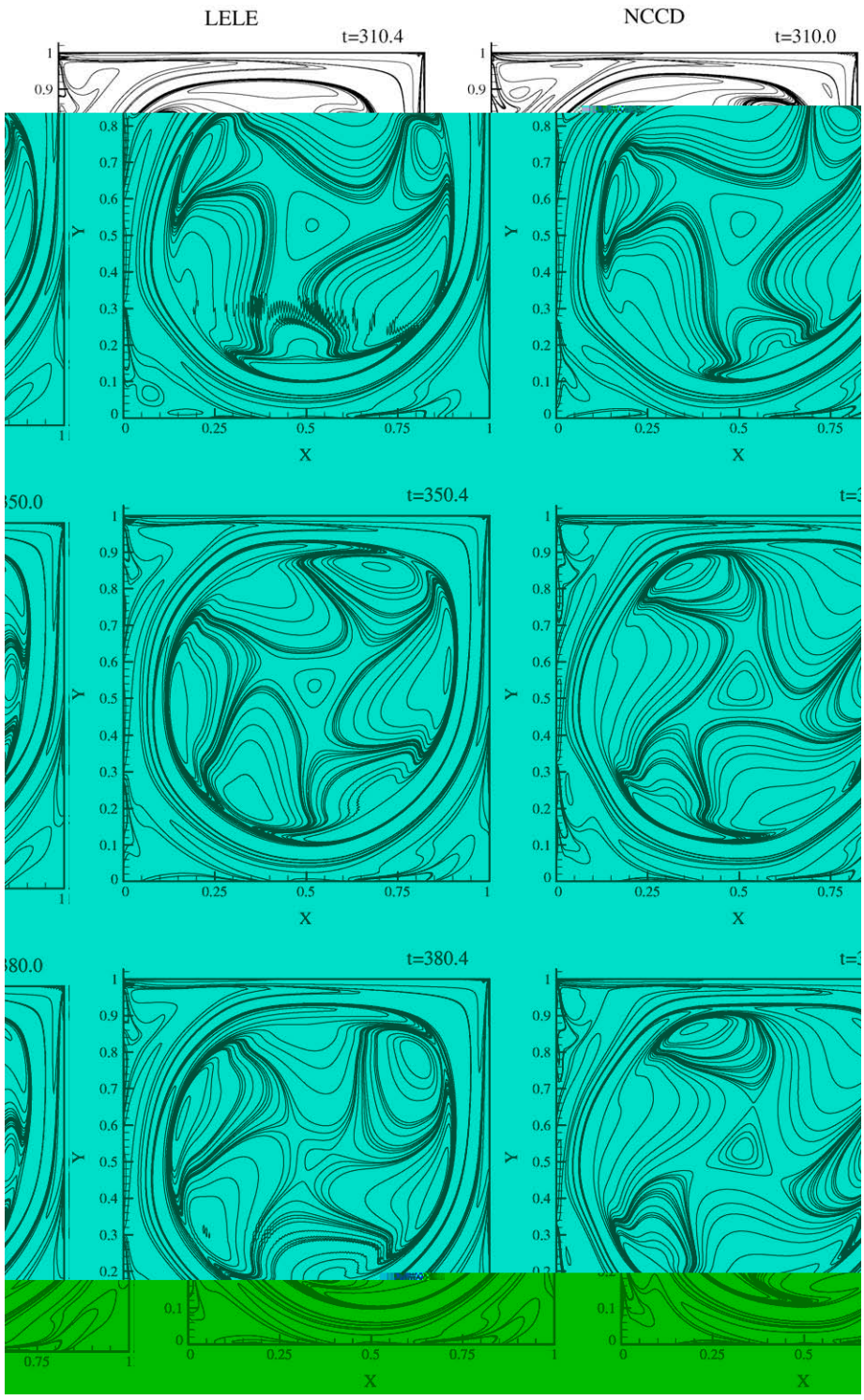

Fig. 9. Comparison of vorticity contours in a lid-driven cavity problem, at various time frames solved using Lele's scheme for second derivatives and the NCCD scheme on a grid of size (257×257) for $Re = 10,000$.

results of [28]. The superior ability of the NCCD is clearly evident that with a (129×129) grid, a three significant digit accuracy is obtained. As the grid is further refined, the results improve steadily and with the (257×257) grid a match with [27], up to four significant digit, is achieved for ψ.

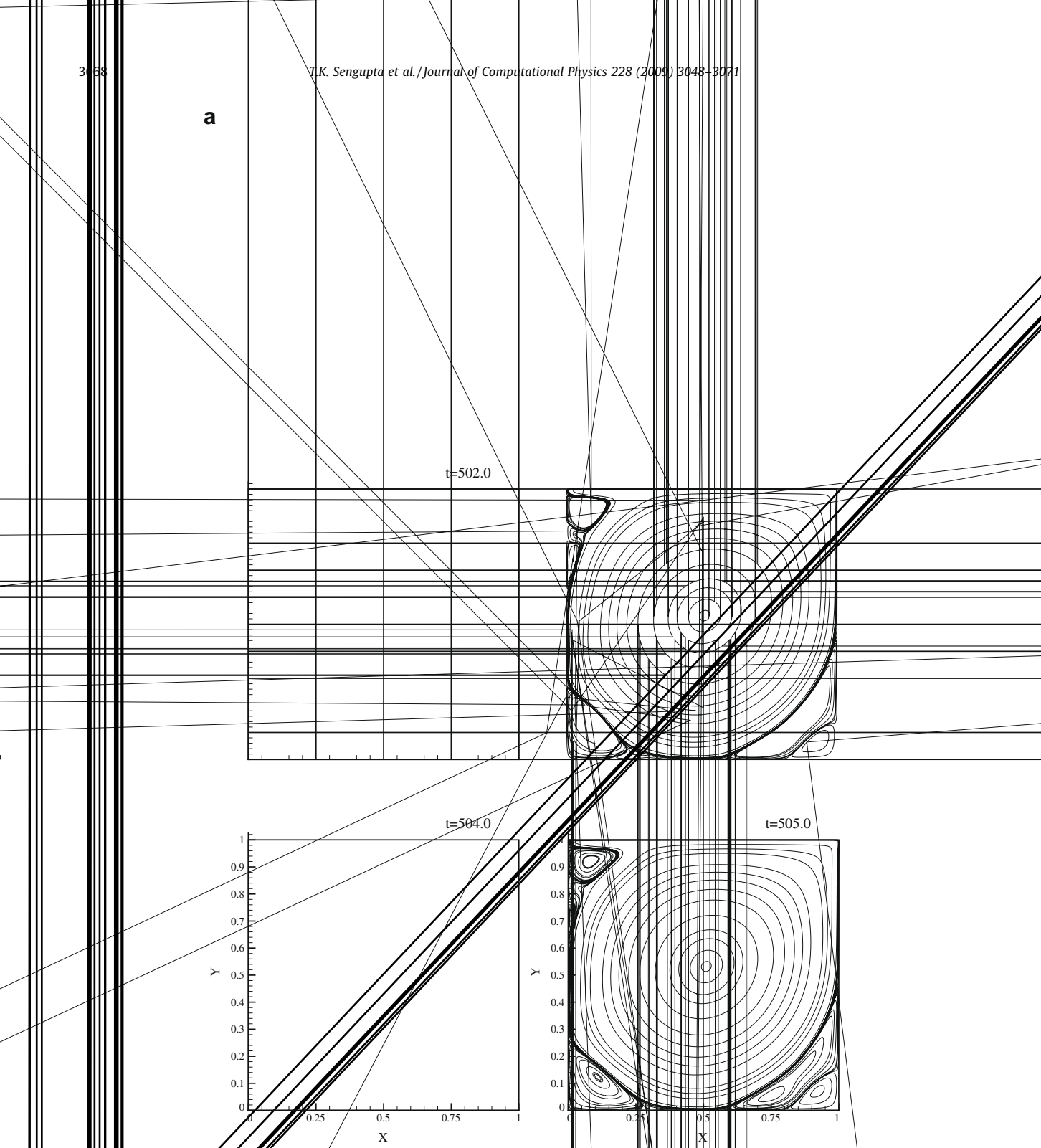

Fig. 10. (a) A full cycle for the stream function contours of the flow in a lid-driven cavity, for $Re = 10{,}000$ at various times, solved using the presented NCCD scheme. The figure shows a good qualitative match with that given in [28]. (b) (i) Evolution of vorticity at (0.95 0.95) for the lid-driven cavity is plotted against time and (ii) the Fourier transform is shown below, identifies the dominant frequencies in the time series.

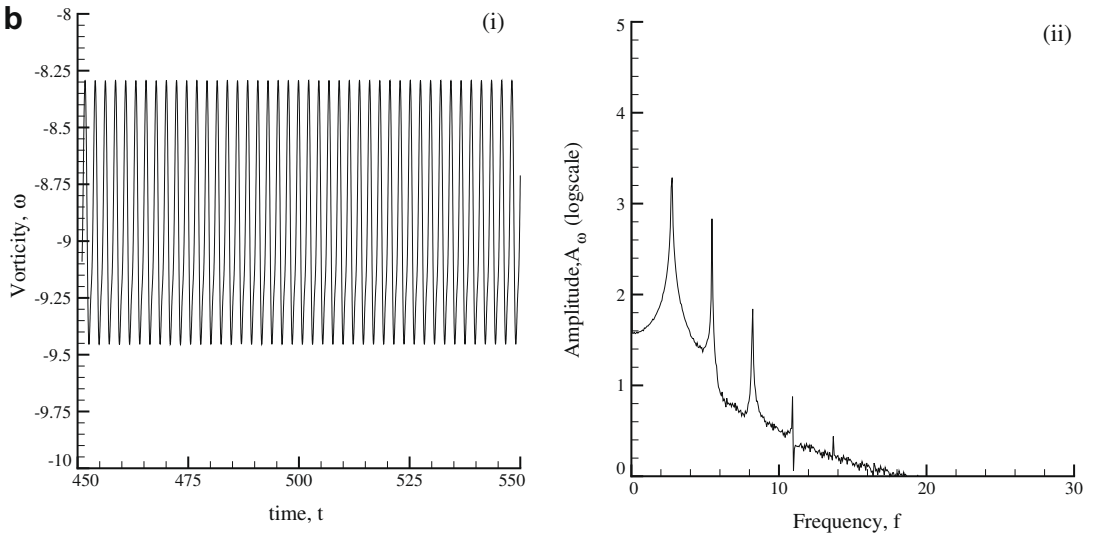

Fig. 10 (*continued*)

vorticity is as given in [26]. The data in Table 2 clearly establishes the viability and accuracy of NCCD for the solution of Navier–Stokes equation.

5.1. The lid-driven cavity problem at Re = 10,000

This problem at the higher Reynolds number is specifically computed for various reasons. Firstly, the flow is inherently unsteady and this was not clearly explained in Ghia et al. [26]. However, there are many work reported in the literature that investigated this problem to explain flow instability and Hopf bifurcation, see for example [28,30,31] among many other references. To show the effectiveness of combined compact schemes, we have used the NCCD and Lele's scheme to compute this flow. The essential difference in the present exercise is to show the need for proper dissipation discretization and the results in Fig. 9 referring to Lele's scheme uses the method for obtaining the second derivative only. We note that the attempt to use the compact schemes given in [1] for first and second derivative was not successful in obtaining results for the driven cavity problem at high Reynolds numbers. This has to do with the numerical instability at the near-boundary points. Even here to use a combination of OUCS3 (for first derivative) and Lele's scheme (for second derivative), we are forced to use a sixth order filter to avoid numerical instability. We have used the methods for first and second derivatives in reporting the NCCD scheme, as reported here.

Bruneau and Saad [28] investigated the temporal instability of this flow and noted the critical Reynolds number for the onset of periodicity to be in the range of $8000 \leqslant Re \leqslant 8050$. In [30], the critical Reynolds number was reported to be at $Re = 8031.93$, while in [31] the Hopf bifurcation is noted to begin at $Re = 7402 \pm 4\%$. The exact value for the critical Reynolds number depends upon the choice of numerical methods, with the added numerical dissipation and effectiveness of dissipation discretization. In the present computed case with NCCD scheme we note the multi-periodic nature of the vorticity field with time. It is interesting to note that the solution obtained by NCCD scheme obtains a new equilibrium solution that has not been reported before. In this configuration, one notices a triangular vortex at the core, that is encompassed by three secondary vortices as satellites. This is shown for $t = 310$ in the top-right frame of Fig. 9. We have used the solution obtained by NCCD method at $t = 300$, as the initial solution for the results shown in Fig. 9, for Lele's method. The instability is related to lack of effectiveness in dissipation discretization by Lele's method, at high wave numbers – as shown in Fig. 1(a). This is evident from the frame shown for $t = 310$ in the top left corner of Fig. 9, where one notices wiggles near the satellite at the bottom. We note that the solution obtained by the NCCD scheme continues to have this unique configuration of vortices in a periodic fashion. However, results obtained using Lele's scheme for the second derivative show the triangular core to dissipate. This cyclic variation of the vortices in the cavity, as a constellation takes a non-dimensional time interval of eight.

In addition to the cyclic variation of the vortices, one can note another periodic variation that relates to the variations of the corner vortices. This periodic nature of the flow field obtained by NCCD scheme is with a time period of six and a full cycle is shown through the variation of ψ contours in Fig. 10(a). We note that such a cycle of ψ contours were also shown in [28] and they match very well. We note the periodic orbit of the vortices seen for this flow is contributed by the gyration of primary and secondary vortices and that is coupled with the variation of corner vortices. The overall time variation of physical variables are noted in the time series and its FFT in Fig. 10(b). In closing this section, we note that the power of NCCD

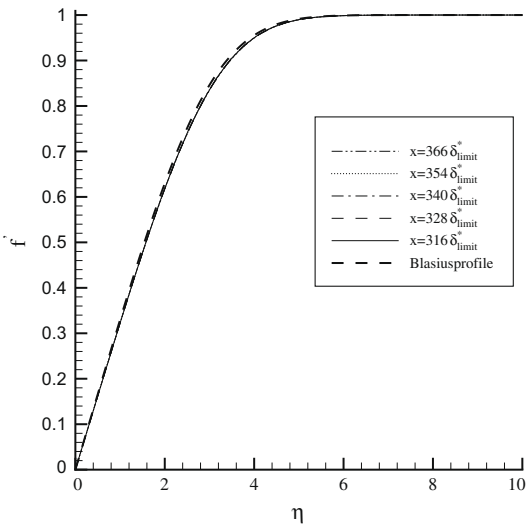

Fig. 11. The Blasius profile developing over a flat plate is shown at different $\times$ locations along the length of the plate for Re = 1081 where Re is based on δ^*_{limit} and freestream velocity. The abscissa represents the similarity variable. A grid of size (600 $\times$ 300) is used with 25 points inside the shear layer.

scheme is such that the results for $Re = 10,000$ is obtained in [28] using a (1024 $\times$ 1024) grid and we obtained the results here using only (257 $\times$ 257) grid points. Using this grid, we are also able to capture the secondary events for the high Reynolds number flow.

6. Simulation of boundary layer development on a flat plate

The flow inside the lid-driven cavity is an intense vortex-dominated flow. Various vortices interfere with the shear layers forming on the walls. A direct application of the compact scheme will not work due to *anti-diffusion* for $j = 2$. As mentioned before, while discussing the results in Fig. 4(a), we actually replace the calculated first derivative at that point by a value calculated using CD_2 scheme. The resultant scheme has also been used to solve for the flow past a flat plate at zero pressure gradient. In Fig. 11, the developed boundary layer is compared with the similarity solution, as given by the solution of Blasius boundary layer. The computed domain is taken such that it begins little upstream of the leading edge of the plate and extends up to a distance of $366\delta*_{limit}$, where $\delta*_{limit}$ is the boundary layer displacement thickness at the end of the domain. The Reynolds number based on the displacement thickness at the outflow is 1081. In the wall-normal direction the domain extends up to $56\delta*_{limit}$. The NCCD needs uniform grid, we have used (600 $\times$ 300) uniformly distributed grid points in the domain. This implies that we have only 25 points inside the boundary layer at the outflow of the domain. Despite such sparse grids, the comparison with the Blasius solution is extremely good.

7. Conclusion

In the present work, we have proposed a new combined compact difference (NCCD) scheme that evaluates first and second derivatives simultaneously. This was motivated by the analysis method developed providing the most essential numerical properties of discrete schemes [3,5] and here it is extended for the CCD schemes. The efficacy of the NCCD scheme is demonstrated by solving few benchmark problems. In particular the following have been achieved:

(1) While the scale resolution property of compact scheme have been reported in literature [1,4,9], other essential numerical properties of schemes have been presented only in [3,5,14] using the full-domain matrix analysis technique. This has been extended here for the CCD scheme of [2], for numerical stability and dispersion properties for the first time. The scale resolution properties of CCD of both the first and second derivatives are compared with other high accuracy schemes in Fig. 1. The stability and dispersion properties for the first derivative are compared for the CCD scheme [2] with the optimized compact scheme, OUCS3 [3] in Fig. 2.
(2) The solution of the 1D convection equation with non-periodic boundary condition are shown in Fig. 3. This reveals numerical instability for the CCD scheme [2] near the inflow due to boundary closure scheme. This is seen from the imaginary part of k_{eq}/k shown in Fig. 4(a). This prompted us to develop a new combined compact difference (NCCD) scheme with stable boundary closure formulae. Improved stability property of NCCD scheme over CCD scheme [2] is shown in

Fig. 4(a) and (b). The improvement brought about for the solution of wave equation near the boundary is shown in Fig. 4(c).

(3) The ability of NCCD scheme in evaluating second derivative is checked by solving the bi-directional convection equation (21) and comparing the results obtained using the method of [1]. The stability property of these two methods and a critical CFL number (N_c^* – below which one obtains perfectly neutrally stable solution) are shown in Fig. 5(a). The solutions of (21) shown in Fig. 5(b), obtained by these two methods are indistinguishable.

(4) We have used NCCD to solve an elliptic PDE – the Stommel Ocean model problem [2]. Displayed solution in Fig. 6 obtained using the present method is indistinguishable from the exact solution [2]. The convergence history of the method with grid size in Table 1 establishes the efficiency and accuracy of NCCD scheme in solving boundary value problems. The computing time required is comparatively very small and up to 10 digit accuracy is obtained using a moderate size grid.

(5) The lid-driven cavity problem is solved here by simulating Navier–Stokes equation in a uniform grid and compared with other published results. The computed solution matches excellently with other benchmark results, obtained using a moderate size grid, establishing NCCD scheme as a valid and efficient tool in solving CFD problems. We have also shown a new equilibrium solution for this flow at $Re = 10,000$ that shows a triangular vortex in the center surrounded by three gyrating secondary vortices as satellites.

(6) Finally, the boundary layer developing over a flat plate with zero pressure gradient is computed to show that a very coarse uniform grid can be used to obtain the Blasius profile. We have only used 25 points inside the shear layer for the purpose.

Acknowledgments

The authors wish to acknowledge Indo-French Centre for the Promotion of Advanced research (IFCPAR), New Delhi for supporting this research vide their Project No. 3401-1.

References

[1] S.K. Lele, Compact finite difference schemes with spectral-like resolution, J. Comput. Phys. 103 (1992) 16–42.
[2] P.C. Chu, C. Fan, A three-point combined compact difference scheme, J. Comput. Phys. 140 (1998) 370–399.
[3] T.K. Sengupta, G. Ganeriwal, S. De, Analysis of central and upwind schemes, J. Comput. Phys. 192 (2) (2003) 677–694.
[4] C.K.W. Tam, J.C. Webb, Dispersion relation preserving finite difference schemes for computational acoustics, J. Comput. Phys. 107 (1993) 262–281.
[5] T.K. Sengupta, S.K. Sircar, A. Dipankar, High accuracy schemes for DNS and acoustics, J. Sci. Comput. 26 (2) (2006) 151–193.
[6] Q. Zhou, Z. Yao, F. He, M.Y. Shen, A new family of high-order compact upwind difference schemes with good spectral resolution, J. Comput. Phys. 227 (2) (2007) 1306–1339.
[7] L. Brillouin, Wave Propagation and Group Velocity, Acad. Press Inc., New York, 1960.
[8] L.N. Trefethen, Group velocity in finite difference schemes, SIAM Rev. 24 (2) (1982) 113–136.
[9] D.W. Zingg, Comparison of high-accuracy finite-difference schemes for linear wave propagation, SIAM J. Sci. Comput. 22 (2) (2000) 476–502.
[10] Y. Ma, D. Fu, Supercompact finite difference method (SCFDM) with arbitrary high accuracy, Comput. Fluid Dyn. J. 5 (2) (2006) 259–276.
[11] K. Mahesh, A family of high order finite difference schemes with good spectral resolution, J. Comput. Phys. 145 (1998) 332.
[12] M.Y. Shen, Z.B. Zhang, X.L. Niu, A new way for constructing high accuracy shock-capturing generalized compact difference schemes, Comput. Methods Appl. Mech. Eng. 192 (2003).
[13] R. Vichnevetsky, J.B. Bowles, Fourier analysis of numerical approximations of hyperbolic equations, SIAM Stud. Appl. Math. 5 (1982).
[14] T.K. Sengupta, A. Dipankar, P. Sagaut, Error dynamics: beyond von Neumann analysis, J. Comput. Phys. 226 (2007) 1211–1218.
[15] Yu.I. Shokin, The Method of Differential Approximation, Springer-Verlag, Berlin, 1983.
[16] D. Durran, Numerical Methods for Wave Equation in Geophysical Fluid Dynamics, Springer-Verlag, New York, 1999.
[17] H.O. Kreiss, J. Oliger, Comparison of accurate methods for the integration of hyperbolic equations, Tellus 24 (1972) 199–215.
[18] D. Estep, A modified equation for dispersive difference schemes, Appl. Numer. Methods 17 (1995) 299–309.
[19] D. Grifiths, J. Sanz-Serna, On the scope of the method of modified equation, SIAM J. Sci. Statist. Comput. 7 (1986) 994–1008.
[20] R. Warming, R. Hyett, The modified equation approach to the stability and accuracy analysis of finite difference methods, J. Comput. Phys. 14 (1974) 159–179.
[21] J. Crank, P. Nicholson, A practical method for numerical evaluation of solutions of partial differential equations of the heat conduction type, Proc. Cambridge Philos. Soc. 43 (1947) 50–67.
[22] J.G. Charney, R. Fjortoft, J. von Neumann, Numerical integration of the barotropic vorticity equation, Tellus 2 (1950) 237–254.
[23] T.K. Sengupta, Fundamentals of Computational Fluid Dynamics, Universities Press, Hyderabad, India, 2004.
[24] A. Dipankar, T.K. Sengupta, Symmetrized compact scheme for receptivity study of 2D transitional channel flow, J. Comput. Phys. 215 (2006) 245–273.
[25] H.A. Van Der Vorst, Bi-CGSTAB: a fast and smoothly converging variant of Bi-CG for the solution of nonsymmetric linear systems, SIAM J. Sci. Statist. Comput. 13 (2) (1992) 631–644.
[26] U. Ghia, K.N. Ghia, C.T. Shin, High-*Re* solutions for incompressible flow using the Navier–Stokes equations and a multigrid method, J. Comput. Phys. 48 (1982) 387–411.
[27] O. Botella, R. Peyret, Benchmark spectral results on the lid-driven cavity flow, Comput. Fluids 27 (4) (1998) 421–433.
[28] C.-H. Bruneau, M. Saad, The 2D lid-driven cavity problem revisited, Comput. Fluids 35 (2006) 326–348.
[29] S.K. Pandit, J.C. Kalita, D.C. Dalal, A fourth-order accurate compact scheme for the solution of steady Navier–Stokes equations on non-uniform grids, Comput. Fluids 37 (2008) 121–134.
[30] M. Sahin, R.G. Owen, A novel fully-implicit finite volume method applied to the lid-driven cavity problem: Parts I and II, Int. J. Numer. Methods Fluids 42 (2003) 57–88.
[31] Y.-F. Peng, Y.-H. Shiau, R.R. Hwang, Transition in a 2-D lid driven cavity flow, Comput. Fluids 32 (2003) 337–352.